LINKING CHEMICAL CHANGES IN SOOT AND POLYAROMATICS TO CLOUD DROPLET FORMATION

A Thesis

by

LAURA ELIZABETH MASON

Submitted to the Office of Graduate Studies of
Texas A&M University
in partial fulfillment of the requirements for the degree of

MASTER OF SCIENCE

August 2009

Major Subject: Atmospheric Sciences

LINKING CHEMICAL CHANGES IN SOOT AND POLYAROMATICS TO CLOUD DROPLET FORMATION

A Thesis

by

LAURA ELIZABETH MASON

Submitted to the Office of Graduate Studies of
Texas A&M University
in partial fulfillment of the requirements for the degree of

MASTER OF SCIENCE

Approved by:

Chair of Committee,	Sarah D. Brooks
Committee Members,	Don Collins
	William H. Marlow
Head of Department,	Kenneth P. Bowman

August 2009

Major Subject: Atmospheric Sciences

ABSTRACT

Linking Chemical Changes in Soot and Polyaromatics to Cloud Droplet Formation.

(August 2009)

Laura Elizabeth Mason, B.S., Texas A&M University

Chair of Advisory Committee: Dr. Sarah Brooks

Soot and other products of incomplete combustion play an important role in the chemistry of the atmosphere. As particles are exposed to trace gases, such as ozone, their chemistry and physical properties can be altered leading to changes in their optical properties, as well as their cloud condensation nuclei and ice nucleation abilities. These alterations can lead to changes in the global radiative budget and cloud microphysical processes, which in turn affect the climate. In this study, the chemical and physical changes associated with the oxidation of pyrene, anthracene, and carbon (lampblack) by ozone were investigated. Fourier Transform Infrared Spectroscopy was used to identify oxidation products and track reaction progress for these representative aerosols. A C=O band attributed to a carboxylic acid formation was observed for all three substances, at each level of exposure to ozone - 20 ppm, 40 ppm, and 80 ppm. Second order reaction rate constants ranged from 9.58×10^{-16} cm^2 $molecules^{-1}$ s^{-1} to 7.71×10^{-13} cm^2 $molecules^{-1}$ s^{-1}. Measurements of water uptake, ice nucleation efficiency, and optical properties were obtained to determine whether any physical changes associated with the oxidation process occurred. Optical measurements show an increase in the ultra-violet

absorption of anthracene, but not for pyrene, while an increase in the visible absorption for pyrene was observed, but not for anthracene. Oxidized soot froze at a warmer temperature (-22.8°C) then fresh soot (-25.6°C), showing an increase in ice nucleation efficiency. Our data indicates that oxidation by ozone does alter the chemistry and physical properties of the substances study, leading to possible changes in how they interact with atmospheric processes.

ACKNOWLEDGEMENTS

I would like to thank my committee chair, Dr. Sarah Brooks, and my committee members, Dr. Don Collins and Dr. William Marlow, for their guidance and support throughout the course of this research.

I would like to thank my research group members, Adam Fornea, Naruki Hiranuma, and Andy Glen, for all their helpful ideas and assistance with this study. I thank the Department of Atmospheric Science faculty and staff for making my time at Texas A&M University a great experience. Thanks go to Rick Littleton, from the Texas A&M Microscopy and Imaging Center, for his assistance. I also want to extend my gratitude to the National Science Foundation (NSF) for providing the funding for this study.

Thanks also go to my friends and family for their constant supports, especially my husband Jason. Finally, thanks to my mother and father for their encouragement and love that has kept me going for the past 25 years. I also want to thank God for blessing me with my family and the desire to learn more about the world around us.

TABLE OF CONTENTS

LIST OF FIGURES

FIGURE Page

LIST OF TABLES

1. INTRODUCTION

Soot and other products of incomplete combustion that are released into the atmosphere play important roles in atmospheric chemistry and the climate. These particles can alter radiation budgets, as well as the microstructures of clouds, which in turn affects the climate. Aerosols can serve as sites for heterogeneous reactions, absorb and scatter solar radiation, and can act as cloud condensation nuclei (CCN) or ice nuclei (IN) [*Finlayson-Pitts and Pitts*, 2000] . Increases in biomass burning and fossil fuel consumption have led to increased concentrations of soot and polycyclic aromatic hydrocarbons (PAHs) [*Seinfeld and Pandis*, 2006]. These increases make these particles an active area of atmospheric research. Not only is the earth's climate affected by products of incomplete combustion, PAHs have been shown to be toxic to human health [*Finlayson-Pitts and Pitts*, 2000]. As these particles reside in the atmosphere they react with atmospheric trace gases, this process is commonly referred to as aging or oxidation. These reactions can change the aerosol's hygroscopicity and optical properties, as well as their toxicity [*Finlayson-Pitts and Pitts*, 2000; *Rudich*, 2003]. The physical and chemical complexities of soot and other organic by products of incomplete combustion make these particles difficult to study [*Kwamena and Abbatt*, 2008; *McCabe and Abbatt*, 2009; *Poschl*, 2005], therefore more research is needed.

Soot is a complex substance and its structure can depend on its fuel source and

---

This thesis follows the style of *Journal of Geophysical Research.*

combustion conditions [*Chughtai et al.*, 1999]. Figure 1 depicts a fragment of a carbon surface structure as well as a model fragment of an oxidized carbon surface. Soot is mainly produced by anthropogenic activities. It is estimated that carbonaceous particle emissions are in the range of 12-24 Tg yr^{-1} [*Penner et al.*, 1993]. *Lary et al.* [1999] estimates that 10-50% of all tropospheric particulate matter is carbonaceous. Biomass burning and industrial activity are the main contributors to the anthropogenic emissions of soot. Diesel fuel and coal combustion are the principal sources of soot by fossil fuel emissions [*Penner et al.*, 1993]. Burning of savannahs, forest, agricultural waste, and wood are all sources of carbonaceous aerosols due to biomass burning [*Liousse et al.*, 1996]. Soot's interaction with existing cloud droplets will lead to a decrease in cloud albedo by absorbing radiation [*Rosenfeld*, 2000], while soot activating as CCN can lead to an increase in cloud albedo and decreased precipitation [*Rosenfeld*, 2000; *Twomey et al.*, 1984].

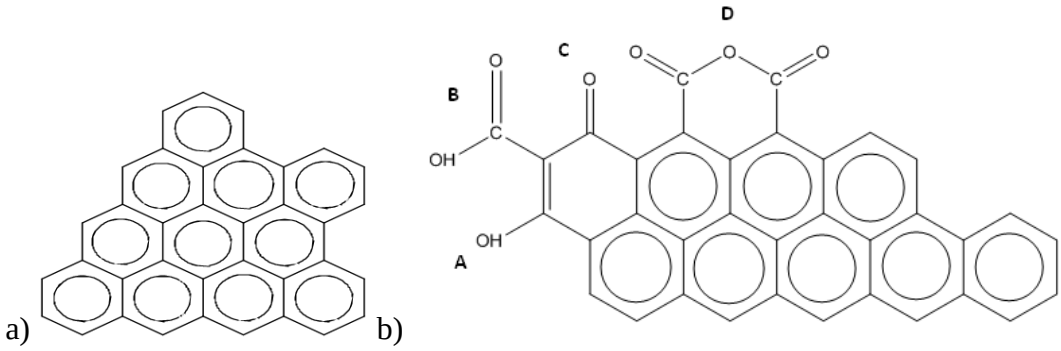

Figure 1. Model fragments of fresh and oxidized carbon surfaces. a) model fragment of a carbon surface b) model fragment of an oxidized carbon surface with acidic oxygen surface functional groups: a) phenolic b) carboxyl c) quinonoid d) anhydride originating from neighboring carboxyl groups.

Freshly emitted soot is hydrophobic, but as soot interacts with atmospheric trace gases, such as ozone, it becomes more hydrophilic [*Chughtai et al.*, 1991; *Weingartner et al.*, 1997; *Zuberi et al.*, 2005]. *Chughtai et al.'s* [1991] Fourier Transform Infrared Spectroscopy (FTIR) studies show formation of polar acidic functional groups, known as carboxylics, on the surface of soot after oxidation by ozone. Figure 1b illustrates some of the possible functional groups that form on oxidized soot. These formations possibly explain the increase in the concentration of the soluble components of soot. *Decesari et al.* [2002] found that soot oxidation causes the formation of water soluble polycarboxyclic compounds or humic like substances (HULIS). HULIS have been shown to decrease the surface tension of cloud droplets, which in turn influences cloud microphysics and radiative properties [*Facchini et al.*, 2000]. The above studies show how aged soot can become hydrophilic, leading to studies that show that aged soot can

act as CCN as well as IN [*Kotzick and Niessner*, 1999; *Poschl*, 2005]. Previous studies explored the kinetics of the ozone-soot reaction as well as the PAH-ozone reaction [*Chughtai et al.*, 1991; *Decesari et al.*, 2002; *Perraudin et al.*, 2007b]. While most of these studies examined the bulk reaction, our goal was to examine surface reactions [*Chughtai et al.*, 1991; *Kotzick and Niessner*, 1999].

Combustion particles can be chemically altered by PAHs adsorbed on the particle's surface, changing the particle's chemistry and water uptake abilities, making the chemistry of these substances atmospherically relevant [*Seinfeld and Pandis*, 2006]. PAHs are formed by incomplete combustion of fossil fuels and biomass burning. Ninety percent of PAH emissions into the atmosphere are anthropogenic [*Finlayson-Pitts and Pitts*, 1986]. Atmospheric PAHs occur in the form of gases (2 ring), solids adsorbed/absorbed to the surfaces of aerosol particles (>5 ring), and semi volatile compounds that are distributed between the gas and particle phases (3- 4 ring PAH) [*Finlayson-Pitts and Pitts*, 2000]. Figure 2 illustrates the structure of pyrene and anthracene, the two PAH compounds chosen for this study. Anthracene is the smaller of the two with a molecular mass of 178 g/mol and consists of three fused benzene rings. Pyrene has a molecular mass of 202 g/mol and has four fused benzene rings.

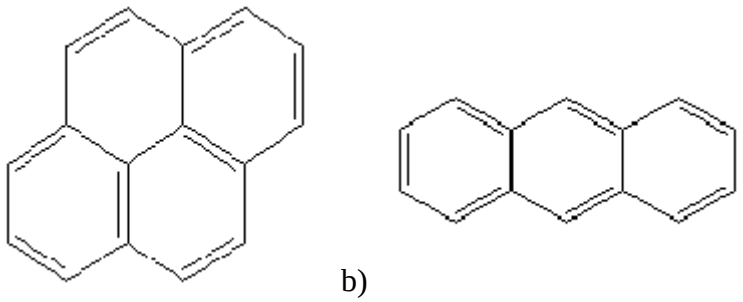

Figure 2. Structures of PAHS a)pyrene and b)anthracene.

PAHs are known to have carcinogenic, mutagenic, and allergenic potential to humans. Studies have shown that when they undergo atmospheric processes, such as reactions with ozone, their products are even more toxic [*Calvert*, 2002]. Past studies of PAHs have explored homogenous gas-phase reactions, PAHs in gas phase with O_3 and NO_x, and heterogeneous surface reactions, PAH bound to a surface with atmospheric trace gases [*Finlayson-Pitts and Pitts*, 2000]. The latter studies are important to cloud microphysical properties because the chemical reactions could alter the aerosols hygroscopicity and may enhance their CCN ability [*Kotzick et al.*, 1997]. Studies have looked at the kinetics of PAH/ozone reactions as well products formed [*Kwamena et al.*, 2006; *Perraudin et al.*, 2007a], but due to different methods and the complexity of each individual substance possible comparisons between studies can be difficult. *Perraudin et al.* [2007b] studied kinetics of numerous PAHs on the surface of graphite particles and silica particles. They compared their surface reaction rates to gas-phase reaction rates and found that no matter the nature of the particle, particulate PAH concentration, and

gaseous ozone concentration, surface reactions are more rapid than most gas-phase reactions and are atmospherically relevant. For example, *Perraudin et al.* [2007b] reported $2.4\pm.7\times10^{-17}$ and $1.9\pm7.4\times10^{-17}$ cm^3 $molecule^{-1}$ s^{-1} , for phenanthrene and fluoranthene respectively , while *Kwok et al.* [1994; 1997] conducted gas-phase reactions of ozone with the gaseous phenanthrene and fluorene and reported reaction rates of $4.0\pm\times10^{-19}$ and 2×10^{-19} cm^3 $molecule^{-1}$ s^{-1}, respectively. While studies have been conducted on the chemistry and kinetics of PAHs reactions with ozone, very little has been conducted on the hygroscopicity of such PAHs. This study explores the hygroscopicity of soot and common PAHs before and after their oxidation.

In order to gain a better understanding of how soot and PAHs affect the atmosphere, we need a basic understanding of how these substances individually interact with atmospheric trace gases. The primary goal of this study was to observe the surface oxidation of soot and PAHs by gaseous ozone. Fourier Transform Infrared Spectroscopy (FTIR) was used to identify oxidation products and track reaction progress for these representative aerosols. The secondary goal of the study was to assess how observed chemical changes in the aerosol alter physical properties of the aerosol and their impact on cloud formation processes and climate. Samples of fresh soot and PAH and those that had undergone exposure to 80 ppm of ozone for 24 hours were analyzed by three additional techniques to look for any changes in the aerosols' optical properties, hygroscopicity , and ice nucleation activity due the ozone exposure. These techniques are described below.

Using FTIR we identified the chemical changes occurring at the surface due to the reaction of ozone with our substances. Kinetics of the surface reaction of O_3 with carbon (lampblack) and two PAHs; pyrene and anthracene, have been calculated.

Optical properties of these aerosols were also of interest, therefore changes in ultra-violet and visible (UV/VIS) absorption upon oxidation where explored. Changes in optical properties of an aerosol can alter the radiation budget, which in turn affects the climate.

Hygroscopicity was explored in order to determine if the aging process of these products led to more hydrophilic substances. Hygroscopicity refers to a particle's wettability; particles can be hydrophobic, unwettable, or hydrophilic, wettable Hygroscopicity is an important characteristic of atmospheric aerosols, since it indicates the atmospheric conditions required for the aerosols to take up water and become solutions. Chemical reactions with gas phase oxidants occur faster in solutions then in solid form, therefore hygroscopicity changes can alter atmospheric lifetimes of aerosols. Water uptake alters the particles optical properties which can have an impact on atmospheric visibility [*Hiranuma et al.*, 2008]. Hygroscopicity alters the ability of aerosols to act as cloud condensation nuclei (CCN). CCN are defined as aerosols which can serve as nuclei upon which water vapor can condense[*Wallace and Hobbs*, 2006]. While hygroscopicity is not a direct measurement of CCN activity, an aerosol's ability to act as a CCN depends not only on its water uptake abilities, but its physical and chemical properties as well. If our substances, which are hydrophobic before oxidation became

hydrophilic after they reacted with ozone, they would have a better chance of acting as CCN or IN.

IN are aerosols which can serve as nuclei upon which ice crystals can form, but unlike CCN, an IN can initiate the freezing process by different mechanisms. Gaining a better understanding of ice formation in the atmosphere is important. Mainly because the release of aerosols into the upper troposphere may increase the efficiency of cirrus cloud formation and cause significant changes in the Earth's radiative budget [*IPCC*, 2007]. Ice nucleation can occur in two ways, heterogeneously and homogenously [*Wallace and Hobbs*, 2006]. Homogeneous freezing occurs at very low atmospheric temperatures; pure water cloud droplets are expected to freeze at or below -40°C. Pure water is uncommon in the atmosphere and therefore crystals of pure ice rarely form. Ice is formed through either homogeneous freezing of a solution or by heterogeneous freezing. Heterogeneous freezing occurs when an aerosol serves as a site for water to freeze to. Heterogeneous freezing can occur by condensation freezing, immersion freezing, contact freezing, and deposition freezing [*Lynch*, 2002; *Vali*, 1985]. Many ice nucleation measurement techniques do not discriminate between mechanism [*Bertram et al.*, 1996; *Onasch et al.*, 1999; *Rogers*, 1988]. In this experiment, we were able to set up the experiment to study the mechanism we were interested in, currently we can study contact or immersion freezing. Contact freezing is defined as the freezing of a supercooled droplet that occurs due to contact with an IN at the droplet's surface. Immersion freezing is defined as the freezing of a supercooled water that occurs due to an IN suspended in the body of water [*Lynch*, 2002; *Vali*, 1985]. The ability of oxidized

soot particles to act as IN were measured in this studied and compared to previously reported IN efficiency of fresh soot.CCN and IN formation process occur under different conditions and it's important to study both mechanisms of cloud development.

In this study, we employed four separate analytical techniques, horizontal attenuated total reflectance infrared spectroscopy (HATR), UV-VIS spectrophotometer, environmental scanning electron microscope (ESEM), and an ice microscope apparatus. Collectively these measurements provide insight on how the surface chemistry of aerosols influences their ability both to uptake water and to act as ice cloud nuclei.

2. EXPERIMENTAL METHODS

2.1 FTIR-HATR Kinetic Experiments

The oxidation of pyrene, anthracene, and carbon (lampblack) are monitored in real time by horizontal attenuated total reflectance (HATR-IR). HATR enables us to use IR spectroscopy to analyze substances by simplifying sample preparation and making it easier for spectral reproducibly. Traditionally samples are scanned by FTIR by grinding the samples and dispersing them into a matrix, a substance that is IR transparent. This process is time consuming and the quality of the measurements can be adversely affected. ATR allows the samples to be directly placed on the crystal with very little sample preparation. ATR measures the changes that occur in the totally internally reflected infrared beam when the beam comes into contact with a sample. An infrared beam propagates through an optically dense crystal with a high refractive index at a certain angle. As the IR beam is internal reflected it creates an evanescent wave that extends beyond the surface of the crystal. The evanescent wave penetrates into the sample in contact with the crystal a certain depth [*Harrick,* 1967]. This depth depends on the wavelength of the light, the refractive index of the crystal, the incident angle of the IR beam, and the refractive index of the sample. The evanescent wave will be attenuated or altered in the infrared regions where the sample absorbs energy. This altered energy from the evanescent wave is passed back to the IR beam which then exits the opposite side of the crystal where it passes to the detector in the IR spectrometer. The system is then able to generate an infrared spectrum of the substance in contact with the surface. In

order for this technique to be successful, the sample must be in direct contact with the crystal because of the limited range of the evanescence wave and the refractive index of the crystal must be significantly greater than that of the sample or else internal reflectance will not occur. Crystals can be made out of many materials Zinc Selenide (ZnSe) and Germanium are the most common. We chose ZnSe for this study. ZnSe refractive index is 2.4, has a spectral Range of 20000-630 cm^{-1}, and has a pH range of 5-9. However, theoretically ZnSe is not the ideal crystal for studying materials with high refractive indices such as carbon, lampblack or the PAH. Since there is not a significant difference between the refractive indices of the crystal and the substances it comes into contact with total internal reflectance by theory does not occur. In order to obtain total internal reflectance, the angle of incidence must exceed the critical angle defined as:

$$\theta_c = \sin^{-1}\left(\frac{n_2}{n_1}\right) \quad (1)$$

where n_2 is the refractive index of the substances and n_1 is the refractive index of the crystal. In our case we were extremely close to the critical angle which enabled us to still obtain spectra of our substances [*Harrick*, 1967]. Appendix A offers a further explanation of the depth of penetration and how future experiments can be optimized. Traditional ATR design the crystal was placed vertically then the thin sample was clamped to it. Newer setups, like ours, have the crystal horizontal allowing us to measure liquids and solids with little to no preparation. The advantage of the HATR-IR was that it allowed us to obtain spectra of the surface of the substance placed on the crystal while it was being exposed to gas phase concentrations of ozone or other oxidizing agents. We

could obtain kinetic results as well as observe the molecular bonds changing all in real time. Disadvantages of this current setup were the experiment times were 24 hours and the limited volume of the chamber (500 µl) limits the amount and the form that substances can be placed on the crystal. The HATR-IR method similar to ours has been employed to study ozone's reaction with other organic materials [*Dubowski et al.*, 2004; *Hung et al.*, 2005].

Ozone was chosen as the oxidizing atmospheric trace gas due to its high concentration in polluted areas where soot and PAH concentrations are typically the highest. Carbon (Lampblack) from Fisher Scientific was used as our 'soot' particles, chosen due to its accessibility and as a base for future soot research. Anthracene and pyrene (Sigma-Aldrich) were chosen as our representative PAHs. As stated before, the three-four PAH can be in solid or gas phase and both have been measured in particle form in the atmosphere [*Finlayson-Pitts and Pitts*, 2000]. Figure 3 shows our experimental setup. In our experimental set-up, ozone is generated by the HC-30 generator (Ozone Solutions). A tank of oxygen serves as our supply for the ozone generator. Oxygen enters the generator at a flow rate of 0.01 l min^{-1}, controlled by a mass flow controller (Model MC-10SLPM-D(O_2), Alicat), and passes into a corona cell, where the molecular oxygen splits into atomic oxygen, which then reforms to ozone. Ozone is produced at high concentrations 3-28 grams per hour. In order to obtain a steady ozone concentration, part of the ozone flow (0.02-0.08 l min^{-1}) is pulled off prior to the mixing chamber and sent to the vent hood. Once the ozone enters the mixing chamber it is diluted with nitrogen gas (N_2) at a flow rate of 10 l min^{-1}. Nitrogen gas is

provided by a liquid nitrogen cylinder. The flow of N_2 is controlled by a mass flow controller (Model MC-10SLPM-D (N_2)). The mixture of O_3/N_2 gas can be directed either to the vent hood or the HATR chamber. Ozone concentration is measured by an UV absorption analyzer (UV-100, Eco Sensors, Inc, 254 nm). The UV analyzer draws a flow of 1 l min^{-1} from the main line prior to the chamber or vent hood tee. Ozone concentrations of 20 ppm -100 ppm can be generated using this setup. For this study concentrations of 20 ppm, 40 ppm, and 80 ppm were chosen. These concentrations are extreme, when compared to typical atmospheric concentrations of 30 – 40 ppb [*Finlayson-Pitts and Pitts*, 2000]. The HATR chamber (Pike Technologies) is equipped with an inlet and an outlet which allows the O_3/N_2 mixture to interact with the substance place on the crystal. To continuously monitor reaction progress, spectra are collected using a PerkinElmer Spectrum 100 Fourier Transform IR. The PAHs originally were a solid substance; this led to poor contact with the crystal. The spectra associated with these PAHS contained noise and made it difficult to observe the bonds associated with the substances. While we are still able to observe a change occurring as we exposed to ozone the noise caused difficulty in analyzing the data. Figure 4 illustrates the type of spectra obtain from solid pyrene in contact with the crystal.

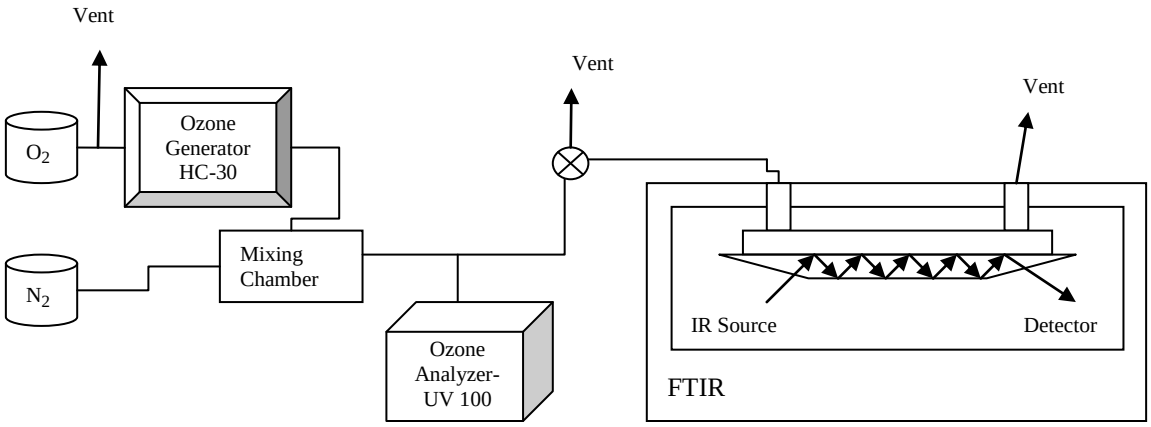

Figure 3. Oxidation experiment setup.

.

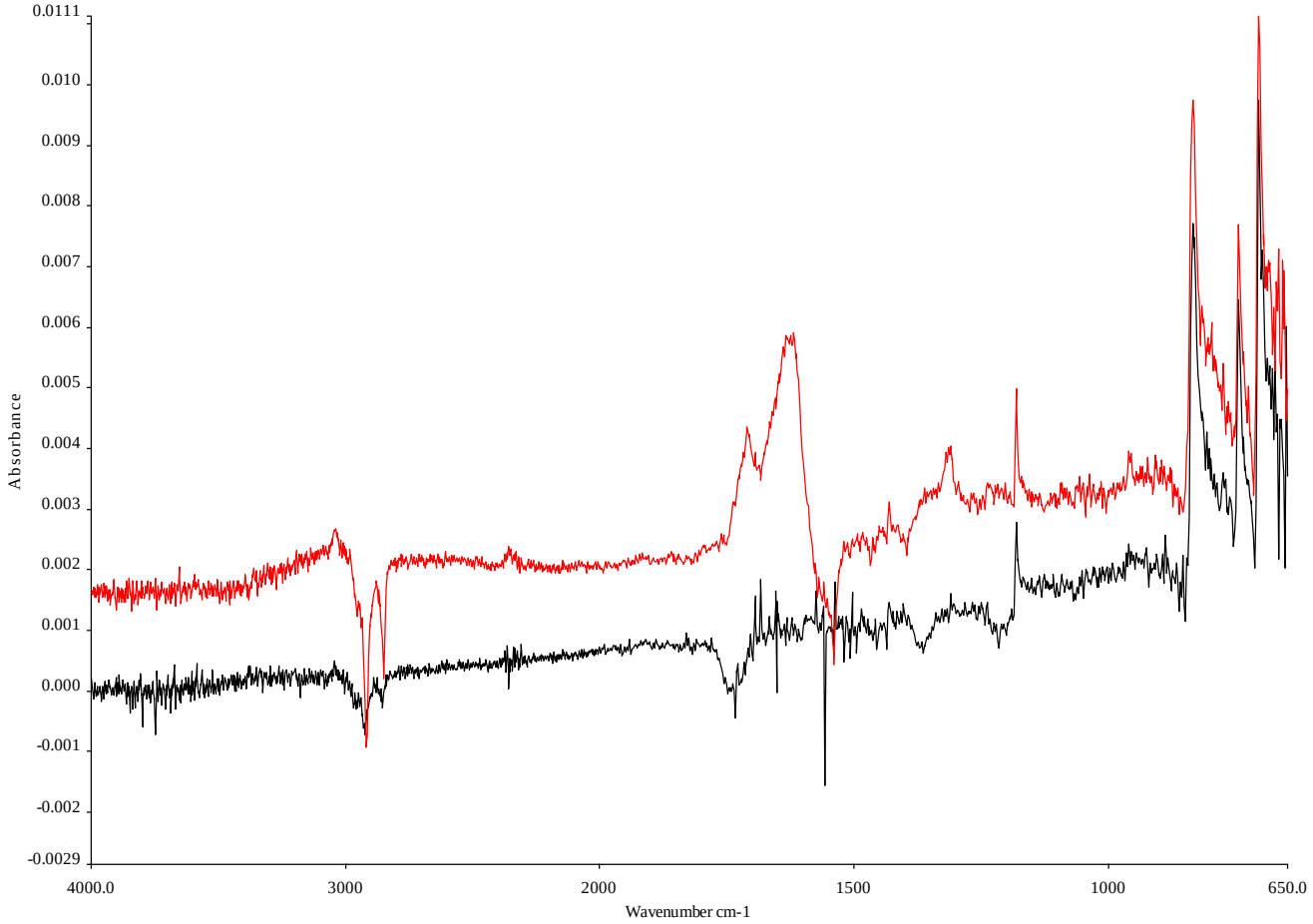

Figure 4. Solid pyrene fresh(black) and oxidized (red).

Not only was noise a problem but the small volume (500 µl) of our HATR chamber limited us on the amount of solid that could be placed on the crystal. Therefore we concluded that our set-up works best for liquids and films, which also provided the best contact with the crystal. Since our substances were crystalline solids they needed to be dissolved. Acetone was chosen as our solvent [*Hung et al.*, 2005]. Both PAHs included in this study were soluble in acetone, and since it has a high vapor pressure the acetone evaporates quickly. Different mixtures of PAH/acetone were generated and scanned to compare the spectra they generated. Our goal was to have the lowest amount of substance but still have a strong PAH spectra. Figure 5 are spectra of pyrene taken at different concentrations. We calculated how many molecules of pyrene it would take to generate a monolayer of coverage on our crystal surface as 5.31×10^{14} molecules/plate, using the cross section area of a pyrene molecule of 1 nm^2 and the surface area of our crystal 5.31 cm^2. For each concentration we determined the number of monolayers created when placed on the crystal, as indicated in figure 5. Figure 5 shows as we decrease the concentration of pyrene the signal of the peaks associated with the bonds in the substance decreases making it increasingly difficult to identify them.

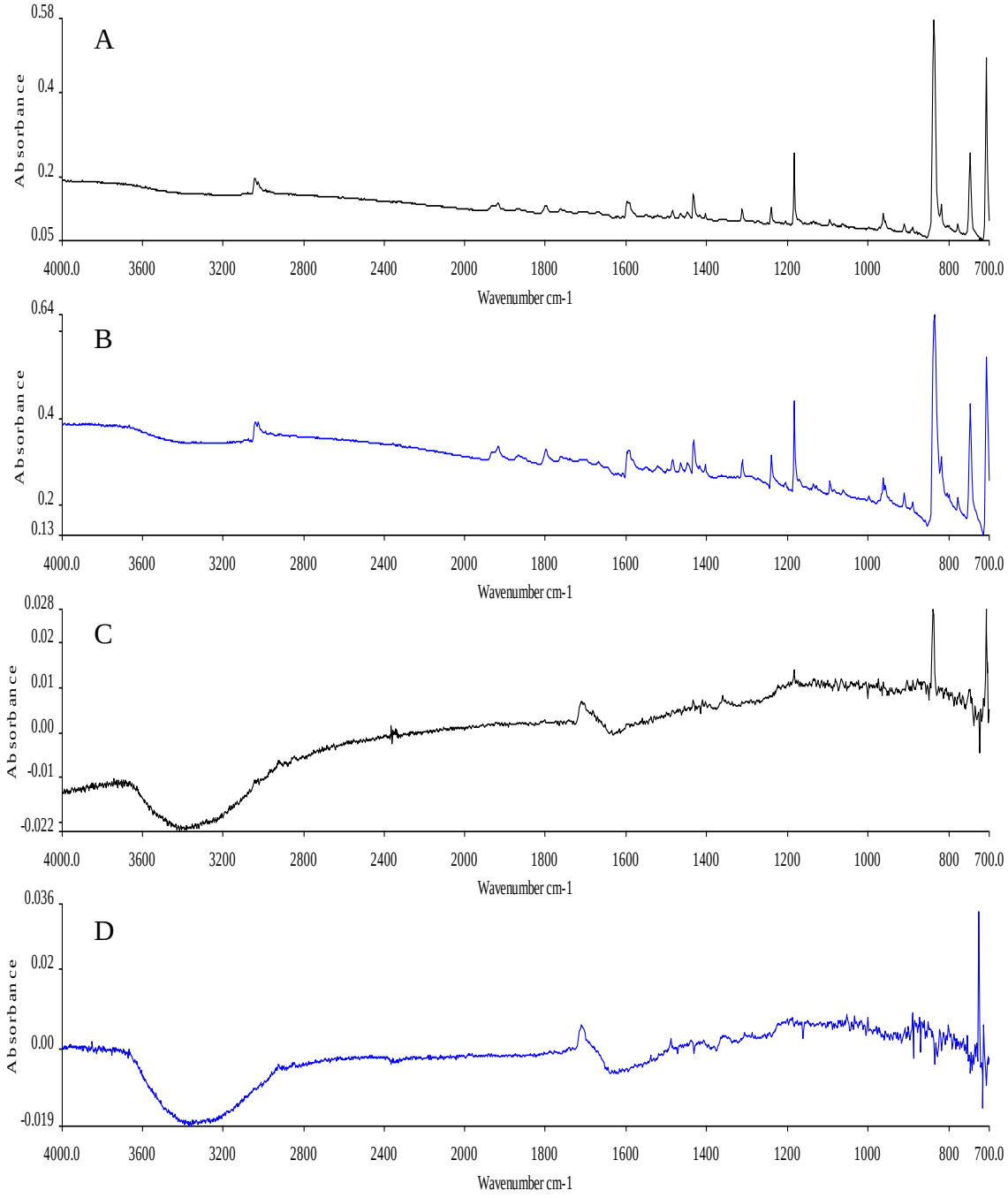

Figure 5. Spectra of pyrene at different concentrations of substance. A is 10 mg/ml (2803 monolayers, B is 1mg/1ml (280 monolayers),C is .2 mg/ml (56 monolayers), and D is .05 mg/ml (14 monolayers).

We chose a concentration of 1mg/ml for all our PAH solutions. It allowed us the lowest number of monolayers but still gave us a strong substance signal to identify the molecular bonds.

Solutions of PAHs were generated by placing a small amount of PAHs in an equal amount of acetone. Solutions were stirred for 20 minutes to allow all the PAH to dissolve in the acetone. This technique can only be applied for the PAH substances, the carbon (lampblack) does not dissolve in acetone. The method for the oxidation of carbon (lampblack) will be discussed below. Once the solution is placed on the crystal, the acetone evaporates and we are left with a thin film of PAH [*Hung et al.*, 2005]. To ensure that all the acetone has evaporated the sample is dried with a 10 l min^{-1} flow of nitrogen for at least 30 minutes. A spectrum of pure acetone was also obtained for comparison and insurance that all the acetone had evaporated prior to the experiment starting. Spectral subtraction was performed to ensure that no peaks associated with acetone were present in the spectra at the beginning of an experiment. It was found that acetone did not chemically alter our PAHs and that their HATR spectra resembled their transmission spectra.

Experiments began with a collection of a background, the clean crystal with a N_2 flow over it. This background was automatically subtracted from the spectra as they were collected by the software (TimeBase, PerkinElmer). Fifty microliters of 1 mg/ml PAH substance was placed on the crystal and dried with a 10 l min^{-1} N_2 flow. Once the sample is dried, we obtained the desired ozone level for the experiment. Once the level was constant we allow the flow of ozone to enter the HATR chamber and the experiment

began. Samples were exposed to ozone for 24 hours. Three experiments at each ozone concentration of 20 ppm, 40 ppm, and 80 ppm were conducted for each of the three substances. Spectra were collected every minute for 24 hours at a resolution of 2 cm^{-1} and from a spectral range of 700-4000 cm^{-1}. Spectra collection began 10 minutes prior to the ozone being allowed to flow into the HATR chamber. Figure 6 illustrates spectrum of each substance studied prior to oxidation. Spectrum A and B are the PAHs, pyrene and anthracene respectively. Spectrum C is carbon (lampblack), our representative soot. Unlike the PAHs, carbon (lampblack) can not go into solution and the PAH HATR setup is not conduisve to measuring the soot like substance. The flow rate of ozone and small volume of the chamber make it diffcult to scan the carbon (lampblack) while it is being exposed to ozone. Using the PAH HATR setup, we did not to observe any changes at the surface of the soot. Since carbon (lampblack) powder was placed directly on the crystal when the N_2/O_3 flow was turned towards the HATR chamber it blew the soot off the crystal. The flow was unable to be altered significantly enough where the soot would remain undistrubed. Therefore, oxidation of our represenitve soot was conducted in a reaction chamber separate from the FTIR instrument.

Thirty milligrams of 250-300 μm sized carbon (lampblack) is placed on the ATR crystal and then scanned at a resolution of 2 cm^{-1} for an average of 5 scans, this is the reference spectrum. Sized soot was obtained by using 3" diameter testing sieves from Newark Wire Cloth Company. The plate housing the crystal and the carbon (lampblack) were placed in a chamber (20 liters) in the hood where ozone could react with it. Since we are no longer scanning while oxidizing, it was no longer feasible to collect spectra every 1 minute. The carbon (lampblack) was exposed to a known (20 ppm, 40 ppm or 80 ppm) concentration of ozone for an hour, removed from the hood and then placed on the IR where it was scanned. This continues for 12 hours, after each hour a spectrum is collected. After the first 12 hour period, the carbon (lampblack) is exposed for 12 straight hours then scanned yielding a spectrum at t=1440 minutes. This gives us a total of 14 data points including the reference scan. Just like the PAHs, three separate experiments are conducted at each level of ozone 20 ppm, 40 ppm, and 80 ppm.

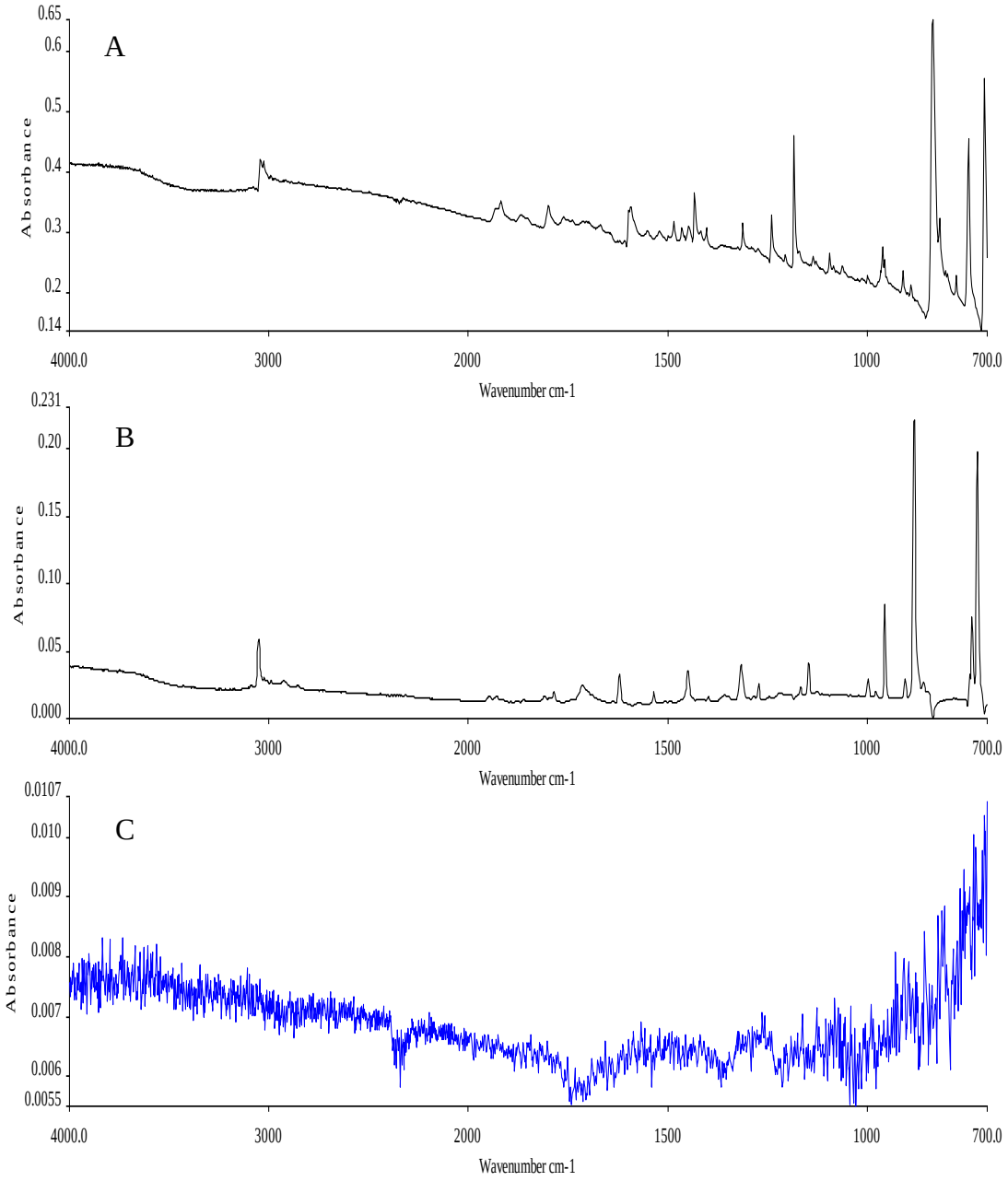

Figure 6. Spectra of pyrene (A), anthracene (B) and carbon (lampblack) (C) taken using the FTIR-HATR setup at 2 cm^{-1} resolution.

2.2 Optical Measurements

Optical properties of the PAHs prior and after oxidation were analyzed by a UV-Visible Spectrophotometer. Fresh and oxidized samples were dissolved in Methanol (Sigma Aldrich, Spectrophotometric Grade, 99%). Solutions of 0.02 mg/ml concentration were generated for each fresh and oxidized PAH. Carbon (lampblack) did not go into solution therefore it was not studied. Oxidized samples were prepared by exposing a small amount of sample to the highest ozone concentration, used during the kinetics experiments 80 ppm (HC-30). All exposures were performed in the fume hood. A 20 mg sample of solid PAH was placed in a Nalgene filter holder, on top of a 47 mm diameter glass fiber filter placed in-between a 250 ml upper chamber and a 250 ml lower chamber. The upper and lower chambers were equipped with inlets and outlets. Ozone entered at a flow rate of 10 l min^{-1} through the top chamber where it filtered through our sample and then exited through the lower chamber. Samples were exposed for a total of 24 hours.

The UV-Visible Spectrophotometer (Model UVmini-1240, Shimadzu) measures the absorption or transmittance of samples in the UV (190 nm-400 nm) and visible (400 nm-700 nm) regions of the electromagnetic spectrum. For these measurements, the instrument was operated in spectrum mode which enabled us to scan a range of wavelengths and obtain a spectrum of the sample being scanned. We measured the absorbance of our samples once from 190 nm-1000 nm at a medium scan speed, giving us a measurement of absorbance every 1 nm. Samples were placed in a cuvet, then place in the sampling compartment of the instrument. The background was corrected using a

pure methanol sample. Correcting the background enabled us to collect spectra of the absorbance due to the PAHs and not the methanol they were dissolved in. One sample for each of the 0.02 mg/ml solutions was scanned according the above parameters and a total of four scans were collected. Absorbance values were recorded from 190 nm – 600 nm, this was the range in which the PAHs absorbed. The instruments accuracy determined our error in our absorbance measurements to be ±0.005 ABS, therefore all reported values are within this range.

2.3 Hygroscopicity Measurements

Hygroscopicity studies were conducted using an ESEM, at the on campus Microscope and Imaging Center. Unlike standard scanning electron microscopy which must be performed under a vacuum environment, the ESEM can be operated under a range of pressures. By controlling the vapor pressure in the ESEM cell, we can use the ESEM to observe a single particle and control the relative humidity (RH) the particle is exposed to. Figure 7 is a photograph of the ESEM instrument.

Figure 7. Photograph of the Electron Scanning Environmental Microscope Lab. The microscope and sealed chamber are located on the left.

When exposed to incremental increases in RH, many substances remain solid until a characteristic RH point is reached. At that point, referred to as the deliquescence relative humidity (DRH), the aerosol will uptake water continuously until it goes completely into solution. The ESEM technique can be used to observe water uptake on individual aerosol particles. In this study, water uptake measurements were conducted on oxidized and fresh particles. Results were compared to determine if the oxidation process had resulted in changes in the deliquescence RH and hydrophillicity of the substances, potentially improving the CCN ability of these substances.

The ESEM technique employed in this study has been characterized prior to our experiment. *Hiranuma et al.* [2008] compared DRH values for sodium chloride, ammonium sulfate, and sodium sulfate from our ESEM method to other various techniques. From Figure 8 we can see that the DRHs reported by *Hiranuma et al.* [2008] agree within our experimental error to results measured with other techniques.

We do note that for each of the three salts, deliquescence was observed by *Hiranuma et al.* [2008] at a slightly lower relative humidity, ~ 3 % less than the RH's reported based on other techniques. *Hiranuma et al.* [2008] proposed that possible reasons for this offset were due to uncertainty in the temperature measurements, uncertainty of the water vapor pressure measurement, and the standard deviation in the measurement. However, an advantage to the ESEM technique is the longer equilibration time (1-3 minutes), compared to other techniques, possible providing us with more accurate results. The three minute equilibration time allows for our temperature to become stable, which in turns gives us a stable RH value. It was concluded that the ESEM technique was an effective method for studying the deliquesce behavior of atmospheric particles. In fact, the ESEM technique has been used by this group [*Hiranuma et al.*, 2008] , as well as others [*Ebert et al.*, 2002; *Krueger et al.*, 2003] to study atmospheric aerosols.

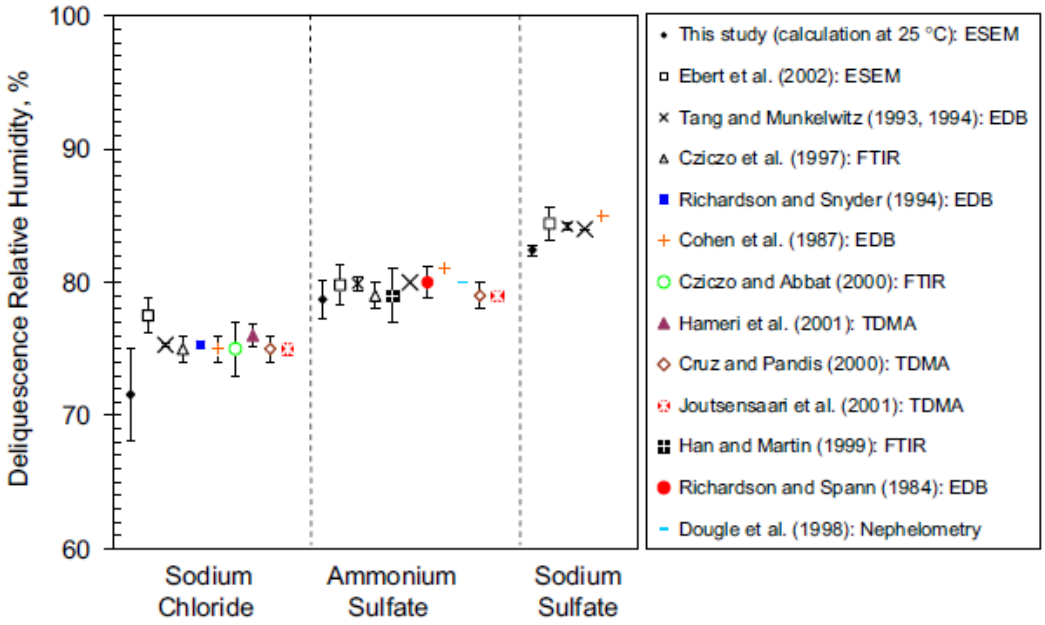

Figure 8. A summary of the deliquescent relative humidites of well known salts by various techniques. Adapted from *Hiranuma et al* [2008]).

In this study, water uptake experiments were conducted on fresh and oxidized samples of pyrene, anthracene, and carbon (lampblack)., following the method developed by *Hiranuma et al.* [2008] three experiments were conducted for each set of oxidized and fresh samples, for a total of 18 experiments. Oxidized samples were prepared by exposing a small amount of sample to our highest ozone concentration, 80 ppm (HC-30). The higher concentration increased the sites available for water uptake. All samples were exposed to ozone in a fume hood, as described in the optical measurements section. Once the samples had undergone 24 hours of exposure, they were placed in an amber color jar to limit light exposure and for easy transport to the Microscope and Imaging Center. Once in the ESEM lab, one to two particles ranging

from 10 µm – 200 µm were placed on an aluminum foil cover stud, and then inserted into the cooling stage located in the microscope chamber. The ESEM microscope chamber allowed us to control the RH by altering pressure inside the chamber and/or the temperature of the stage the sample was placed on.

In this experiment, we set a constant temperature and change the RH by altering the pressure in the chamber. The cooling stage was set to 15 °C. Our ESEM instrument was most stable at this temperature. Since RH is very dependent on temperature, this was also the temperature which produced the minimum fluctuations in RH and greatest accuracy in the experiment. Imaging was also optimized at this temperature, we were able to capture a wide range of pressure settings without having poor picture quality due to large amounts of water vapor. The samples were dried for 30 minutes at 2.5% RH and then the pressure was increased incrementally. The pressure of the chamber can be changed by 0.1 torr, which corresponds to a RH change of 0.7-0.8%. A three minute waiting period occurred at each torr increment, a picture was captured and the diameter of the particle of interest was measured and recorded; this continued until a RH of 100% was reached. At RH's above 96% our temperature became unstable and our images were of poorer quality, therefore images taken after this point had a greater RH variability associated with them. There was too much water vapor in the chamber leading to images in which the particle of interest appeared blurry. At the end of each experiment, the temperature of the area where the sample was placed was measured using a thermocouple. This area was typically cooler then the set temperature. This measured temperature varied for each experiment. Prior to this series of experiments, the

thermocouple was calibrated and an offset of 2.5 K was determined for the thermocouple. All temperature data was corrected for this offset. Obtaining an accurate temperature was important because it was used to calculate the RH our particles were exposed to at that particular torr setting.

At the end of each experiment we calculated the RH under which the particles were exposed using the Clausius-Clapeyron equation shown below:

$$RH(T) = \frac{P}{Ps} \times e^{\left(\frac{Lv}{Rv} \times \left(\frac{1}{273} - \frac{1}{T}\right)\right)} \quad (2)$$

where RH(T) is the RH at a given temperature (%), P is the vapor pressure in the ESEM chamber (torr), Ps the saturation vapor pressure at 273K (= 4.58 torr), Lv is the latent heat of vaporization of water at 273 K (2.5 X 10^6 J K kg^{-1}), T was the temperature of the stage, and Rv is the gas constant (461.5 J kg^{-1}).

Hygroscopic growth factor is defined as the ratio of the particle's diameter at a certain RH and the particle's diameter when dry. $D/D_{0.}$ The measured diameters of the particle recorded at each incremental increase in relative humidity were used to determine the hygroscopic growth factor at each relative humidity. The deliquescence relative humidity, DRH, is the RH at which a deliquescent particle begins to take up water and goes into solution. DRH is determined as the point where the change in the D/Do is the largest over an incremental change in RH. As illustrated by our results below, not all materials have a distinct deliquesce point, instead, many substances such as organic compounds uptake water over a broad range of relative humidites.

Error associated with our DRH measurements was calculated using the accuracy of the pressure control unit and the cooling stage. All instrumental uncertainties were converted to percent relative uncertainties to calculate the RH uncertainty. The pressure control unit is accurate within ±0.01 torr at any given pressure, and the calibration accuracy of the temperature controller is computed as ±0.91 ° (CN90000A series operator's manual). Since we only altered the pressure, the uncertainties varied with the pressure (±0.08-1%), while our temperature was constant (15°C) therefore the percent relative uncertainties were uniform throughout the experiment (±6.08%). The error associated with our RH was calculated using equation (2):

$$\%error[RH] = \sqrt{(\%error[P])^2 + (\%error[T])^2} \quad (3)$$

The absolute uncertainty in RH is found by multiplying the magnitude of the reported RH by the calculated error. The uncertainty in our measurements ranges from ±0.56% - 6.72% RH. The error in our D/Do measurements is the standard error in our measurements, calculated by determining the standard deviation for each substance D/Do measurements and dividing it by the $\sqrt{\#of experiments}$.

2.4 Ice Efficiency Experiments

Recently our group employed a method that allowed us to determine between immersion freezing and contact freezing [*Fornea et al.*, 2009]. In this study we were concerned with when and how oxidized carbon (lampblack) freezes. Due to the hydrophobic nature of fresh soot previous experiments conducted observed freezing by

the contact freezing mechanism. Oxidized soot when placed in contact with the droplet surface would be taken in by the droplet; no clear contact freezing experiments could be conducted. We were unable to determine if the soot was fully immersed in the droplet or if it dispersed throughout the droplet and maintained contact with the droplet surface from the inside.

Ice nucleation efficiency is determined by observing the freezing events of ultra pure water droplets (HPLC grade) inserted with an oxidized carbon (lampblack) particle. Figure 9 illustrates our experimental setup developed by *Fornea et al*. [2009] to observe and freeze IN. In the experimental setup, a tank of dry nitrogen gas provided flow to a Nalgene bubbler, which generated a low humidified flow. This humidified flow passed through the cooling stage of the microscope and prevented droplets from evaporating. The humidified flow consisted of a dry nitrogen flow at 0.57 L min^{-1} and humidified flow of nitrogen at 0.03 L min^{-1}, separately controlled by mass flow controllers (Model MC-10SLPM-D(N_2)). The two flows were mixed together before entering the cold stage at a flow rate of 0.60 L min^{-1}. A dewpoint hygrometer (Model 2000 series DewPrime II, EdgeTech) measured the dewpoint prior to entry into the cold stage. No detectable condensation growth of our droplets was observed due to the additional humidity.

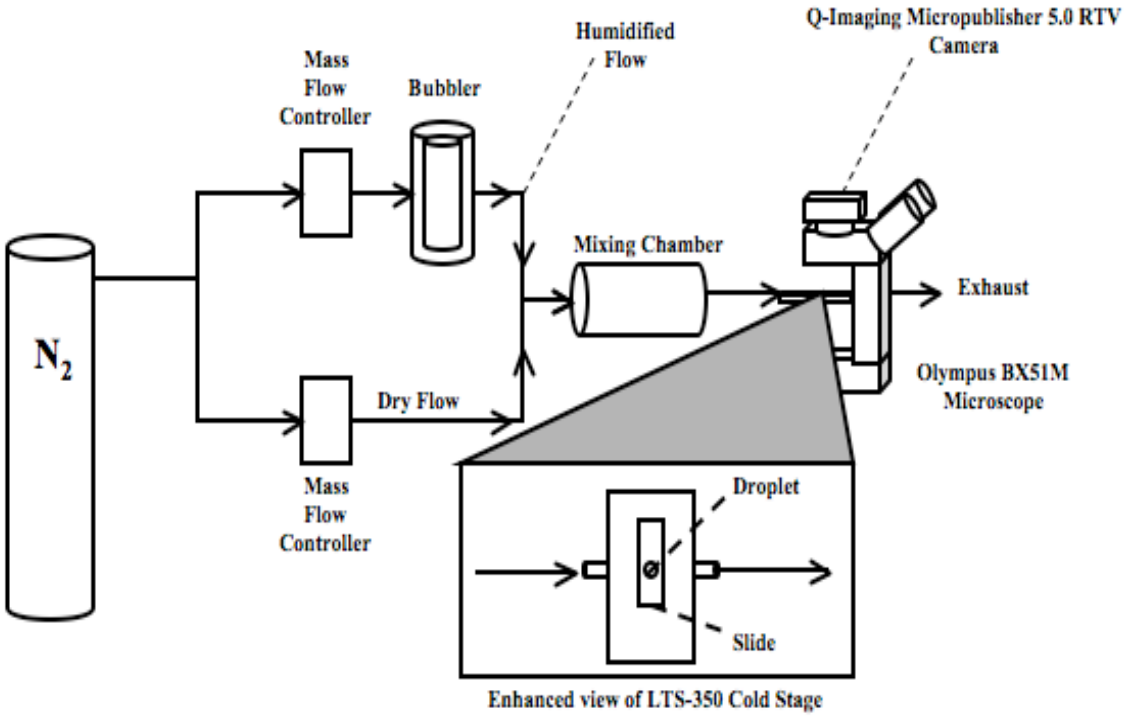

Figure 9. Ice microscope setup. Adapted from *Fornea et al.* [2009].

The cold stage (Model LTS-350, Linkam) is a sealed chamber containing a silanized microscope slide approximately 0.8 mm thick. The surface of the slide was temperature controlled with a sensitivity of a tenth of a degree. The stage was connected to both a temperature controller box and a liquid nitrogen pump, both controlled by software (Model Linksys 32-DV, Linkam). The system acts together to control the flow of liquid nitrogen pumped into the stage during cooling and heating cycles. The stage is attached to an optical microscope (BX51M, Olympus) equipped with a digital camera (Micropublisher 5.0 RTV, Q-Imaging). The digital camera allowed us to monitor the freezing temperatures of the droplets placed on the microscope slide. Images from the

camera were sent to the Linksys 32 software and were captured at a rate of one image ever six seconds. This was sufficient enough to record an image ever tenth of a degree.

Samples were prepared outside of the cold stage. A 2 µl droplet of ultrapure water (HPLC) was placed on a hydrophobic slide, which helped to prevent condensation during the experiment. The specific droplet size was attained by using an Eppendorf micropipettor, which was adjusted to a volume of 2.0 µl. A 250 µm-300µm sized oxidized soot particle was placed in contact with the water droplet. Oxidized samples were prepared in the vent hood, as describe in the optical measurements section, at an ozone concentration of 80 ppm for 24 hours.

The slide was then placed in the sealed cold stage. The temperature was set to decrease from 5 °C to -40 °C at a rate of 1.0 °C/min. Once the -40°C was obtained the software began to warm the stage back up to 5 °C, where a waiting period of one minute occurred before the cycle was repeated. 25 cycles were performed for each experimental setup. A total of 5 experiments were conducted for oxidized soot.

The Micropublisher 5.0 RTV camera recorded images of the droplet during the 25 cycles. The images recorded were used to determine the freezing point of the droplets. Each experiment produces 25 freezing points which we were observed by analyzing the images captured. A freezing event was characterized as a wave of motion through the droplet, a change in opaqueness and reflectivity, and eventual ice appeared. Figure 10 illustrates a typical freezing event. The images presented in the figure were seen as dark droplets due to the oxidized soot dispersing, therefore making it impossible to do discern IN placement.

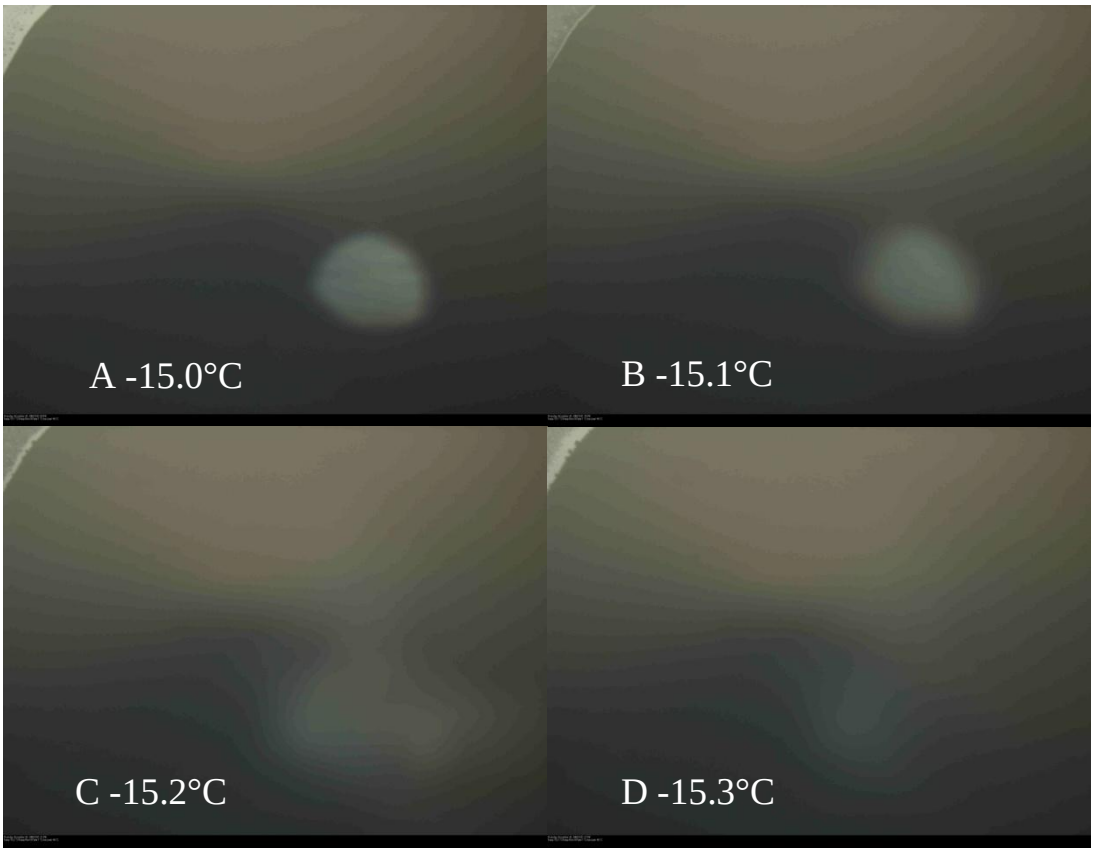

Figure 10. Images of the freezing event of an oxidized carbon (lampblack) particle observed by the CCD camera. The four images are shown in sequential order, panel A is the unfrozen droplet prior to start of the freezing event in panel B. The droplet continues to freeze, which can be seen as the reflective part of the droplet (white spot) begins to disappear in panel C. Panel D is the droplet completely frozen.

By analyzing each image, we were able to accurately identify the freezing temperatures of our droplets. The freezing temperature was acquired from the image in which the reflective part of the droplet completely disappeared (Figure 10d). We observed IN movement during melting and freezing events. Throughout the beginning cycles soot could be seen shifting and dispersing throughout the droplet. This movement increased the variability within a single experiment, while variability's in the individual

carbon (lampblack) particles lead to variability in the freezing temperatures from experiment to experiment.

Fornea et al. [2009] characterized the cooling stage by confirming the melting point of the well documented substance mercury, as well as the freezing temperature of pure water (HPLC grade). Mercury was chosen because its melting point of -38.83°C [*Lide*, 2008] was near the coldest end of our temperature range. A melting point of -39.1 °C with a standard deviation of less than a tenth of a degree was observed. Our setup produced a colder melting point then documented by ~0.3°C. The experiments in which pure water was frozen produced freezing temperatures of -33.1°C with a standard deviation of 0.6°C corresponding directly to the freezing temperatures reported in literature. From this process a temperature uncertainty of 0.2 ºC, as well as, an uncertainty due to human error of the analysis of the images of 0.1 ºC was determined. A maximum uncertainty of ±0.4 °C was calculated by taking the square root of the sum of squares of each individual uncertainty. Therefore all reported freezing temperatures are reported with a maximum uncertainty of ±0.4 °C.

3. RESULTS AND DISCUSSION

3.1 FTIR-HATR Results

Once all the spectra have been collected a difference spectrum was created using the PerkinElmer TimeBase software. Spectrum at t=0, which was the spectrum collected before the ozone is turned on, was subtracted from the spectrum collected at t=1440 minute. Figure 11 is an example of a pyrene subtraction. This subtraction shows us the chemical bonds that have been altered by the reaction with ozone. Experiments showed that a peak forms between 1870 and 1660 cm^{-1} for both pyrene and anthracene. Figure 11 illustrates this peak growth, the top graph contains a spectrum of pyrene from the beginning of the experiment (black) and a spectrum of pyrene from the end of the experiment (green), 24 hours later. Figure 12 are difference spectrum for both pyrene and anthracene. Both spectra illustrate the broad peak, corresponding to a C=O band, which represents carboxylic acid and/or aldehyde compounds forming at the surface. From the difference spectra we determined that the C=O band was formed due to ozone reacting with the PAHs. This band provided a location on which water could bond which could possibly improve the compounds water uptake abilities. This peak was centered around 1744 cm^{-1} for pyrene and 1754 cm^{-1} for anthracene. A similar peak has been reported by others conducting ozone/organic reactions [*Chughtai et al.*, 1991; *Dubowski et al.*, 2004]. Other peaks of interest in the PAHs spectra were the decreases in the C=C band located at 1598 cm^{-1} for pyrene and 1623 cm^{-1}, 1536 cm^{-1} and 1447 cm^{-1} for anthracene. The C=C band was due to aromatic rings in the PAHs stretching. A decrease

in the C-H bands was observed at 841 cm^{-1}, 820 cm^{-1}, 744 cm^{-1}, and 710 cm^{-1} for pyrene, as well as 877 cm^{-1} and 727 cm^{-1} for anthracene. Figure 13 illustrates how these decreases were observed in an anthracene experiment exposed to 40 ppm ozone.

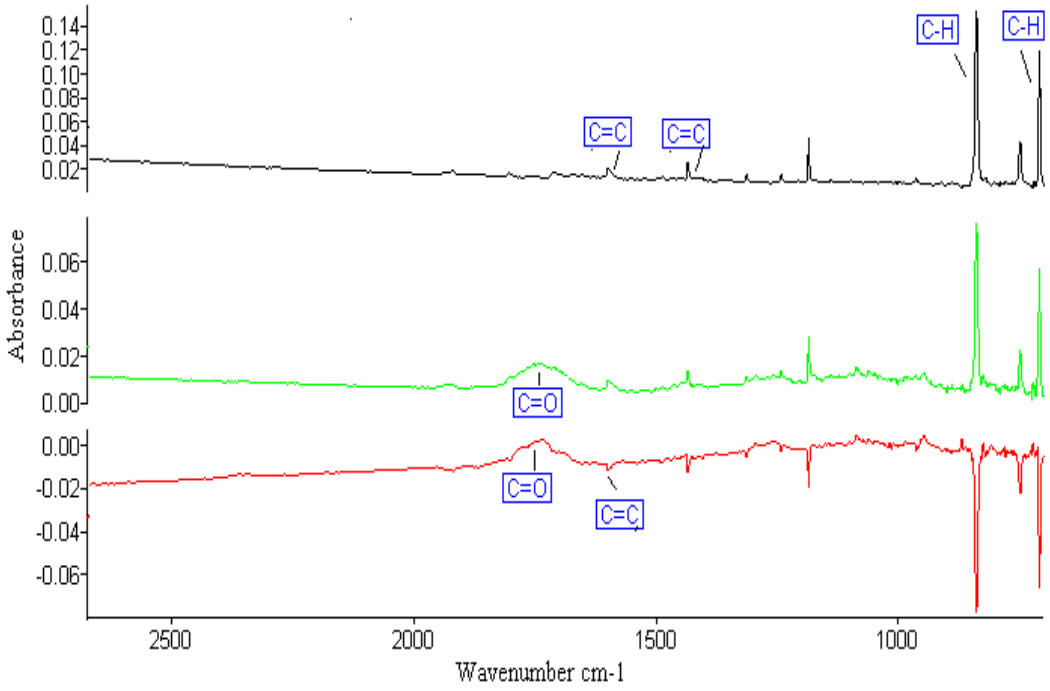

Figure 11. Spectra of pyrene before oxidation (black) and after oxidation (green) for 24 hours at 40 ppm ozone concentration taken at 2 cm^{-1} resolution. The aromatic rings (C=C) and alkenes (C-H) bonds of the PAH can be observed. Difference spectrum (red) taken of the two spectra above. Peaks label at 1744 cm^{-1} represents C=O (aldehyde or carboxylic acid) and at 1598 cm^{-1} represents C=C.

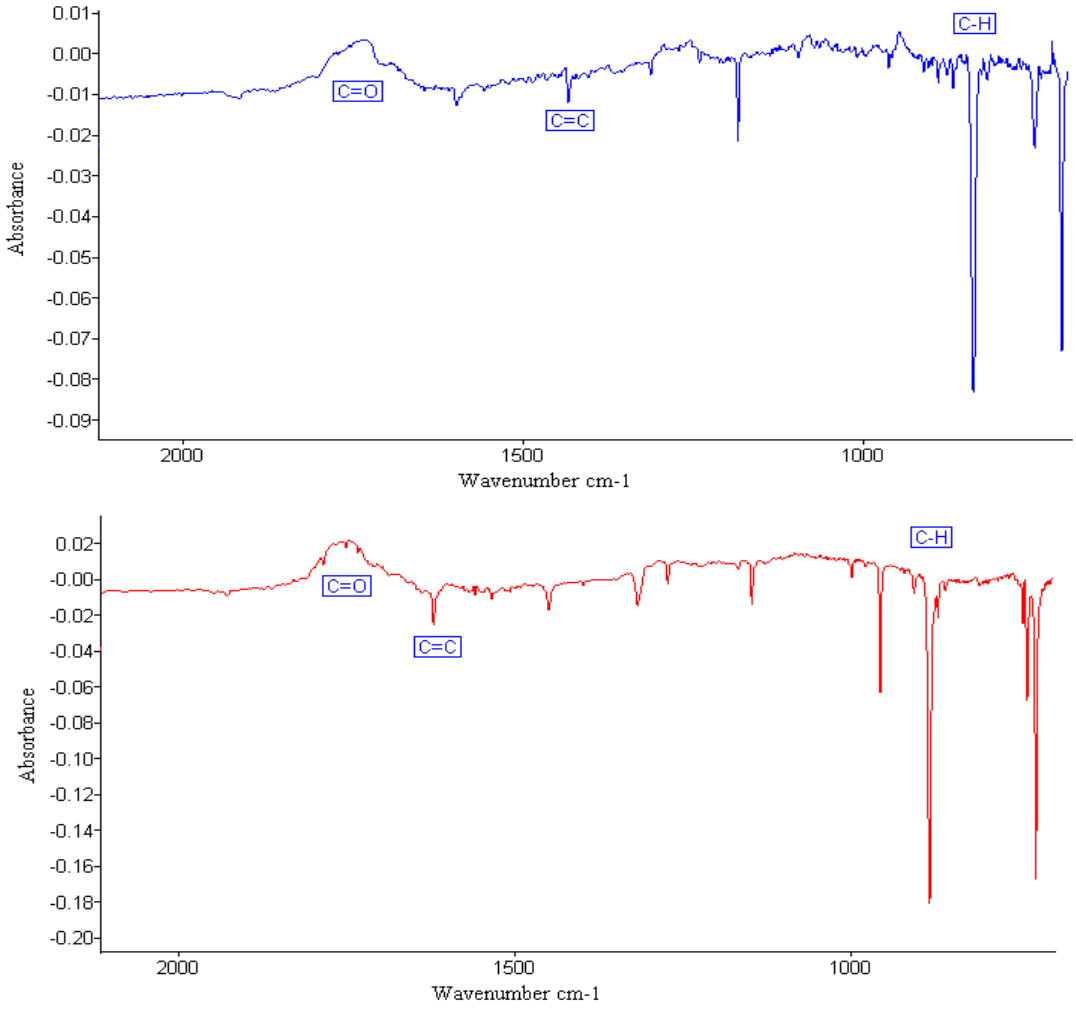

Figure 12. 24 hour difference spectra of pyrene (blue) and anthracene (red). C=O band increases with time.The aromatic rings (C=C) and alkenes (C-H) bonds of the PAH can be observed decreasing with time.

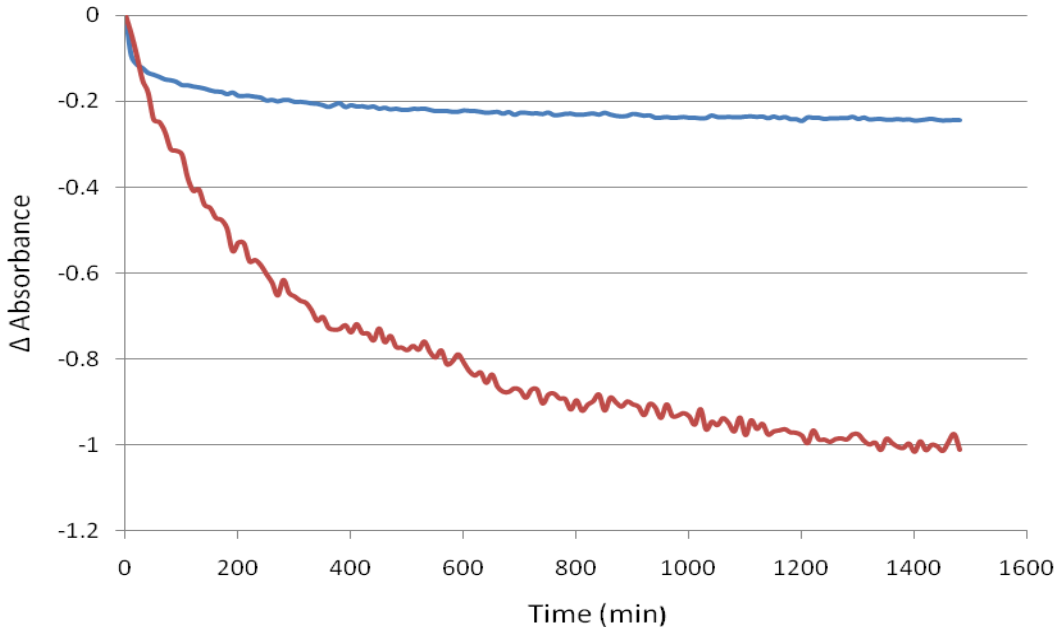

Figure 13. Absorbances changes of the C=C band at 1623 cm^{-1} (blue) and C-H band at 877 cm^{-1} (red).

Carbon's (lampblack) inability to go into solution led to some challenges when oxidizing it as well as analyzing it. Since the substance was in solid form it had poor contact with the crystal, making any molecular bond identification difficult. Figure 14 is a 24 hour difference spectrum of carbon (lampblack). Since soot is a powder moving the sample leads to shifts in the coverage on the crystal therefore noise is created. Even with all the noise we can see a broad peak form, corresponding to the C=O band forming at the surface. For all three substances studied, the same peak associated with the same functional group, a carboxylic acid, formed when exposed to ozone.

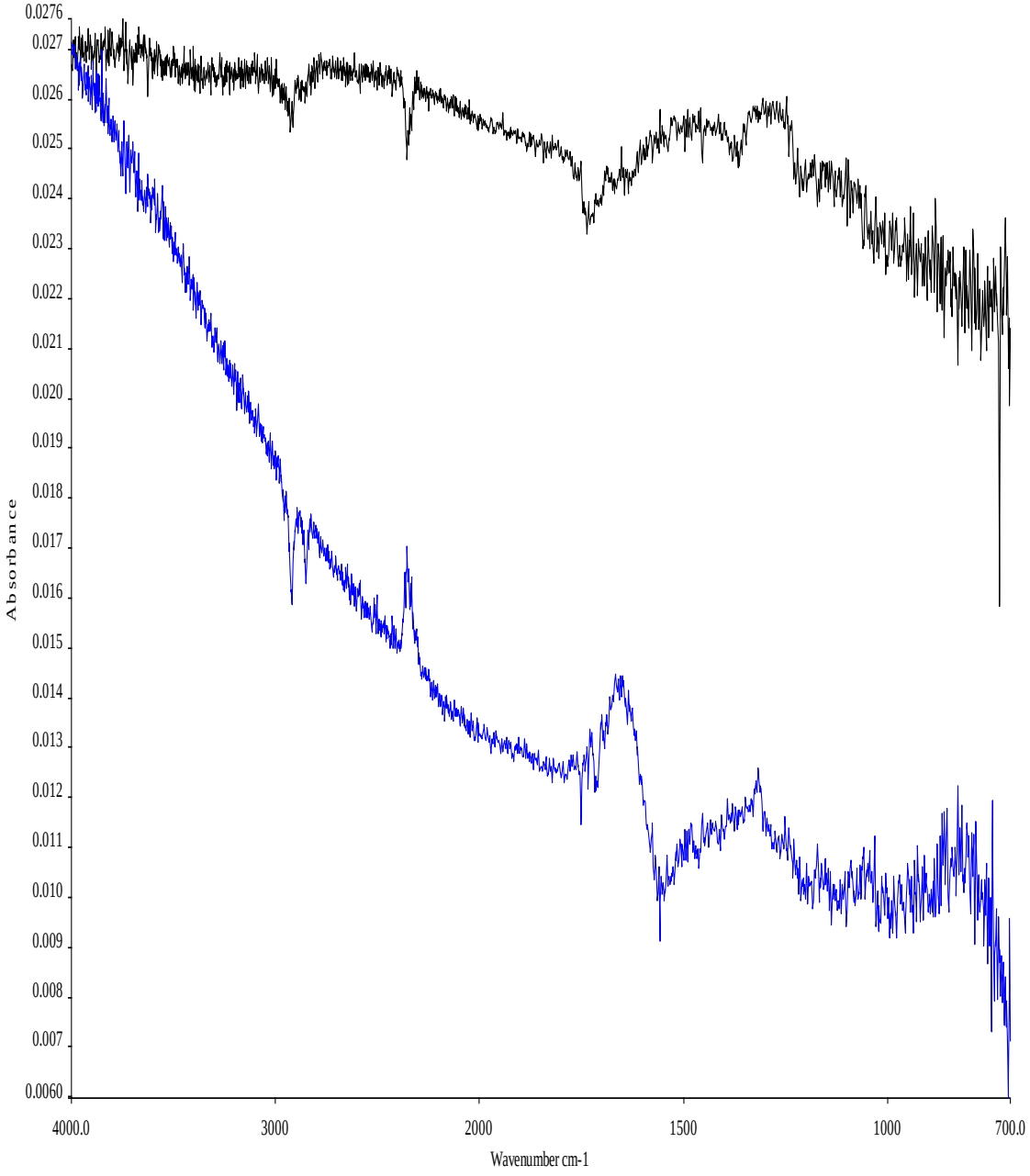

Figure 14. Spectra of carbon (lampblack), fresh (black) and a 24 hour difference spectra (blue).

Using the software provided (TimeBase, PerkinElmer) we calculated the area under the curve from 1865 cm^{-1} to 1659 cm^{-1}, this range incorporates the C=O band for both the pyrene and anthracene. Once we calculated the area for each 1 minute spectra we subtract the reference area from each 1 minute area calculation; then take 10 minute averages of the area differences and plotted them against time. Figure 15 illustrates this for all 9 pyrene experiments. Each experiment exhibited some variations due to the baseline of the instrument shifting over the 24 hour period, as well as the variations in the film coating for each experiment. The ozone concentration varied throughout the experiment as well. While the instrument was set to our chosen values of 80 ppm, 40 ppm, and 20 ppm at any given time the concentration could be ±5 ppm. These ozone concentration variations could be responsible for the different oxidation rates within a set of ozone concentration experiments. For each ozone concentration we averaged the three individual experiments and obtained an individual curve for that concentration. Figure 16 depicts how the area under the C=O band changes with time.

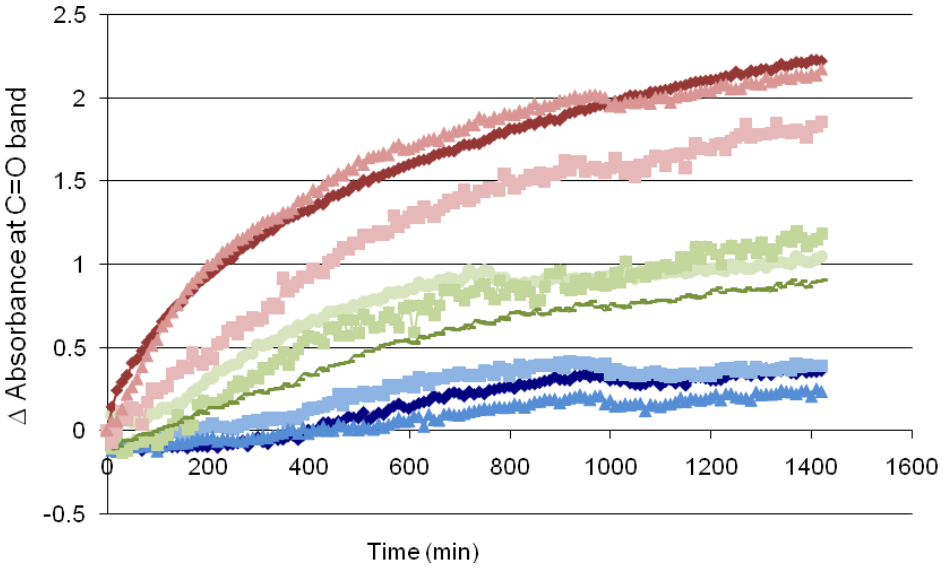

Figure 15. Ten minute averages of Δ absorbance at C=O band for all nine pyrene experiments, red- 80 ppm, green-40 ppm and blue-20 ppm.

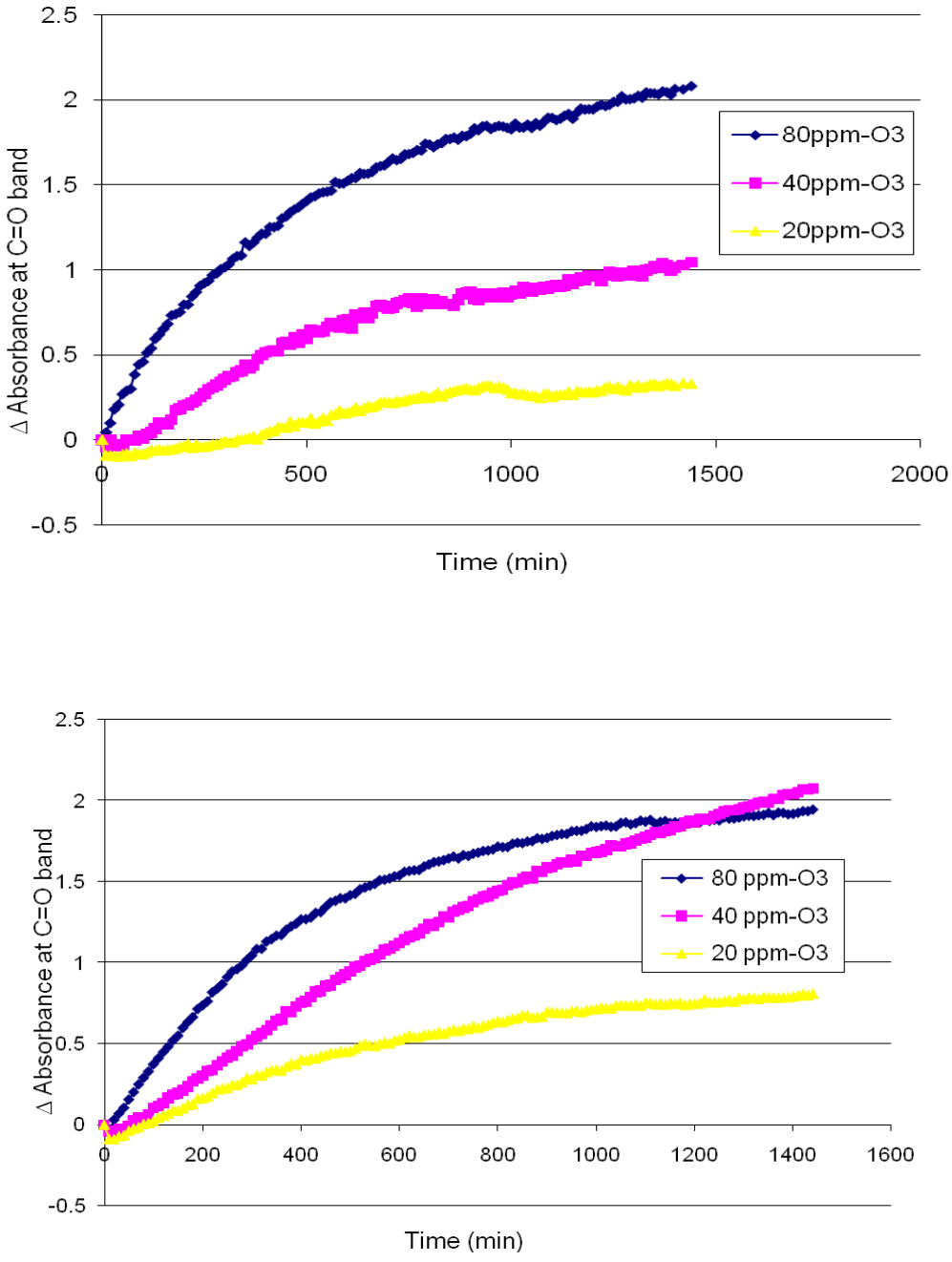

Figure 16. Change in absorbance at C=O band over 24 hour period for pyrene (top) and anthracene (bottom).

From the graphs, we can see the oxidation rates were similar and had relatively the same magnitude for ozone concentrations of 20 ppm and 80 ppm. It also appeared that we had an initial reaction in which we oxidized the first layer of substance followed by secondary reactions occurring at a slower rate. We speculated that secondary reactions were complicated by a number of factors and may include both additional surface reaction and diffusion into the bulk. Calculating the kinetics of the secondary reactions was beyond the scope of this study. However, we were interested in the initial reaction occurring at the surface of our substances. This initial reaction was where the first monolayer of substance was oxidized; therefore our kinetic calculations were for a monolayer surface at this initial rate. In order to determine our reaction rate we fitted our initial reaction data with a linear line. Figure 17, illustrates the best fit linear line for pyrene at each ozone level. For each ozone concentration our time period for the initial reaction decreased with increasing ozone concentration. As with the PAHs, we analyzed the area under the C=O band for soot from 1561 cm^{-1} to 1800 cm^{-1} and averaged the values for each concentration. Figure 18 shows the average C=O absorbance change over time for carbon (lampblack) at each ozone concentration level.

Incomplete information about the coverage on the plate, amount and its geometry, generated uncertainties in our kinetic calculations. It was possible that our coverage was not an evenly spread monolayer but that it island and created an uneven surface as observed by [*Al-Hosney and Grassian*, 2005]for calcium carbonate.

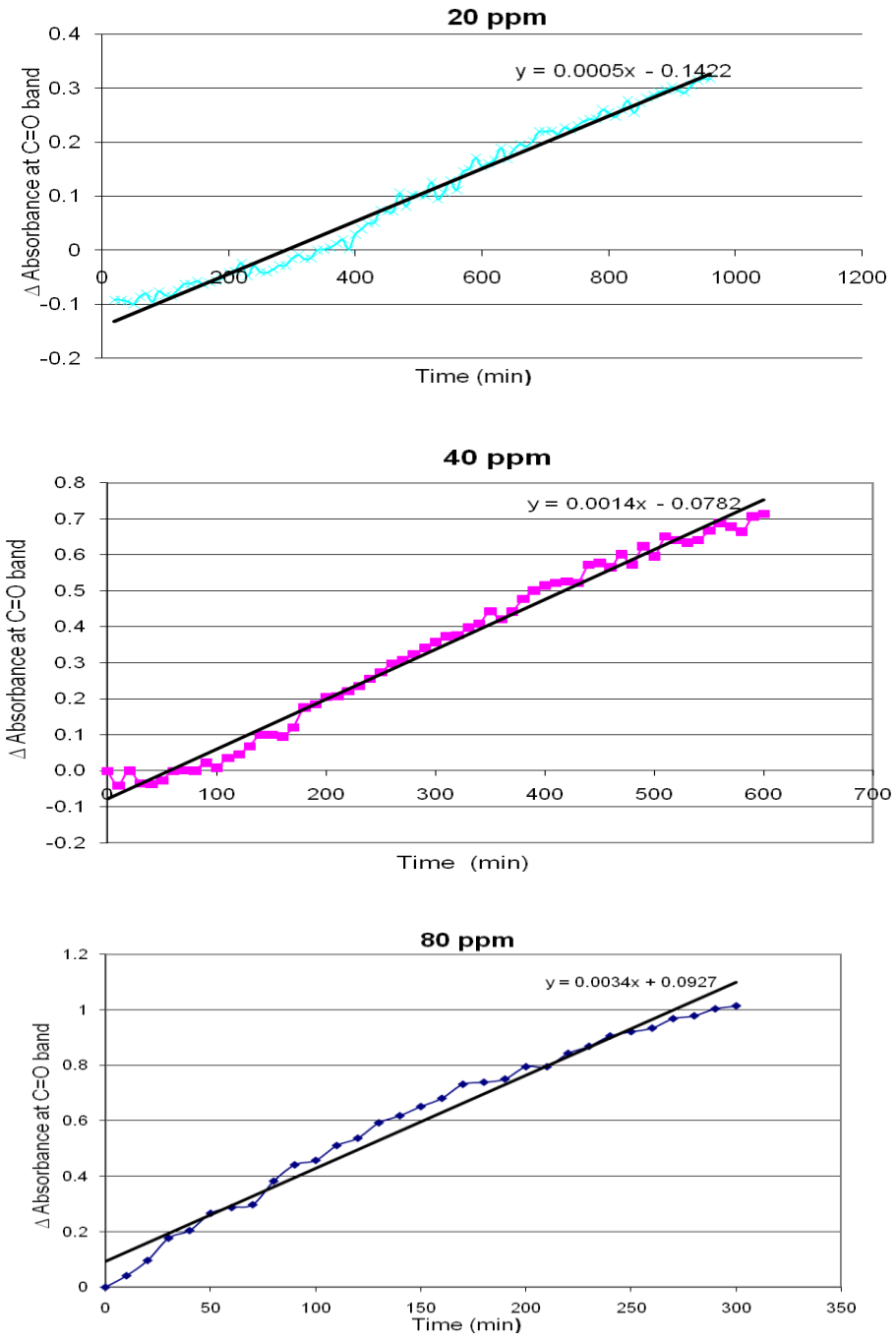

Figure 17. Linear line fits for initial reaction Δ absorbance at C=O band for each ozone concentration for the substance pyrene.

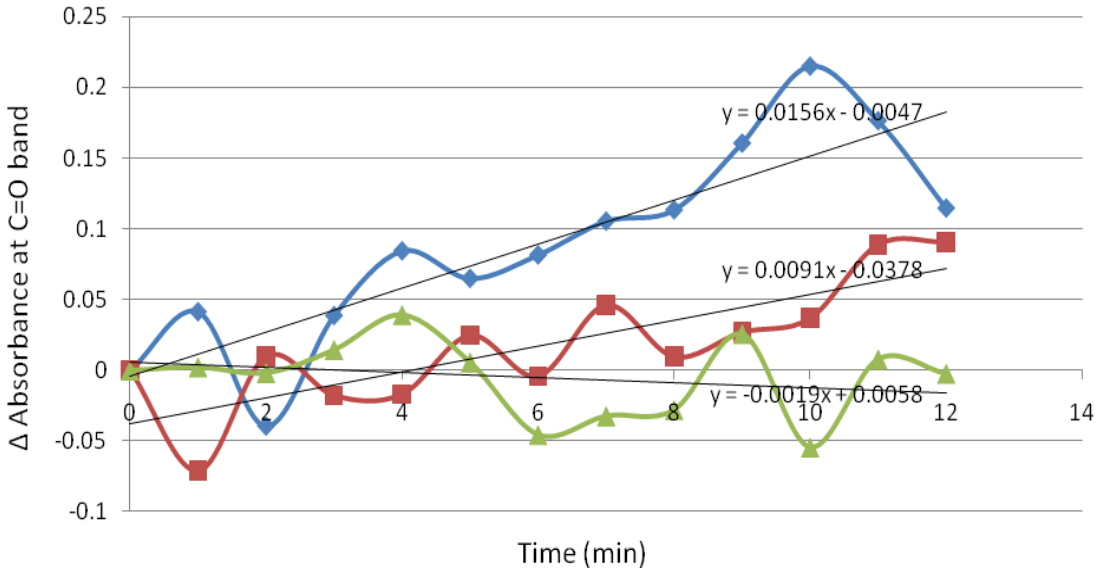

Figure 18. Carbon (lampblack) averaged Δ absorbance at C=O band for 80 ppm (blue). 40 ppm (red) and 20 ppm (green) fitted with linear lines.

3.2 Kinetic Calculations

Kinetics calculations allowed us to compare our results quantitatively to other reported rates of PAH/soot reactions with trace gases. These comparisons also allowed us to determine if our method of observing oxidation was valid as well as possibly determine if these reactions were atmospherically relevant. Beers law tells us that absorbance is proportional to concentration therefore:

$$\frac{abs(C=O)_t}{abs(C=O)_\infty} = \frac{[C=O]_t}{[C=O]_\infty} \quad (4)$$

where $abs(C=O)_t$ represents the C=O absorbance and $[C=O]_t$ is the total surface concentration at time t, at $t = \infty$ is when the initial reaction is complete. The $[C=O_\infty]$ at the end of the initial reaction should be equal to the original surface density of our substance $[SOOT]_0$ or $[PAH]_0$ which turns equation (4) to:

$$[C=O]_t = abs(C=O)_t \times \frac{[PAH]_0}{abs(C=O)_\infty} \quad (5)$$

Surface densities were calculated using the cross section area of the PAHs as 1 nm^2. Assuming we had one monolayer of coverage this yielded a density of 1×10^{14} molecules/cm^2. The average cross section area of our carbon (lampblack) 250µm-300µm diameter particles was 59886 μm^2, giving us a geometric surface density of 1669.82 molecules/cm^2, again assuming one monolayer. Calculations based on the BET surface area measurement of 22 m^2/g [*Popovicheva et al.*, 2008a] carbon (lampblack) were also applied for our soot data. A surface density of 1.52×10^{-4} molecules/cm^2 was obtained by multiplying the BET area by the average amount of soot placed on the crystal, 30 mg.

Since we were observing how the C=O band changes over time we took the derivative of equation (5) which was:

$$\left(\frac{d[C=O]}{dt}\right)_t = \left(\frac{d[abs(C=O)]}{dt}\right)_t \times \frac{[PAH]_0}{abs(C=O)_\infty} \quad (6)$$

To calculate the rate of change of the C=O absorbance, d[abs(C=O)]/dt, we took the derivative of the best fit to the experimental absorbance data which are given for pyrene in Figure 11 and soot in Figure 13. We then calculated a reaction probability (γ), gas-surface reactions are normally treated in terms of γ, which is the fraction of collisions of gas with the surface that lead to a reaction. Therefore in terms of γ the rate of change of C=O was given by:

$$\left(\frac{d[C=O]}{dt}\right)_t = \gamma \times [O_3]_g \sqrt{\frac{RT}{2\pi M}} \quad (7)$$

where $[O_3]$ is the gas-phase ozone concentration (molecules/cm^3), R is the gas constant (8.3145 units J/K*mol), T is the temperature (273 K), and M is the molecular weight of ozone (.048 kg/mol). Combining equations (6) and (7), we obtained an expression for the reaction probability:

$$\gamma = \left(\frac{d[abs(C=O)]}{dt}\right)_t \times \frac{[PAH]_0}{abs(C=O)_\infty [O_3]_g \sqrt{\frac{RT}{2\pi M}}} \quad (8)$$

Table 1 shows the reaction probabilities for all three substances calculated based on equation (8). The reaction probabilities for carbon (lampblack) differ depending on the amount of surface area they had to react with. Reaction probability is expected to be

independent of $[O_3]_g$, because the reaction rate changes linearly with the gas-phase ozone concentration [*Dubowski et al.*, 2004].

Table 1. Calculated reaction probabilities (γ) for all substances at each ozone concentration.

	80 ppm	40 ppm	20 ppm
Pyrene	1.18E-06	1.39E-06	2.22E-06
Anthracene	1.11E-06	8.28E-07	3.17E-06
Carbon (Lampblack)			
Geometric Area	4.80E-14	7.10E-14	1.15E-12
BET Area	1.05E-19	6.46E-21	4.37E-21

Our data shows that γ was dependent on $[O_3]_g$, , and as the C=O band (aldehydes and/or carboxylic acids) was forming there were decreases in the C=C bands (conjugated aromatic rings). If the surface were rapidly oxidized upon collision, the C=C bands would not continue to decrease over time. However as shown in Figure 13 the C=C bands do decrease throughout the experiment. Overall, our observations suggested that the reaction proceeded via two steps. First, ozone must be physisorbed to the surface; second, the ozone chemically reacted with the PAH or soot. Thus, it is appropriate to analyze our data according to the Langmuir-Hinshelwood mechanism. This mechanism refers to the physical adsorption of the gas species to the surface. This treatment assumes that all the adsorption sites have an equal chance of adsorption and the ability of the gas species to bind is independent of whether adjacent sites are occupied or not [*Hunter*,

1993]. Since the ozone cannot be adsorbed onto previously adsorbed ozone, the rate of adsorption (Ra) and rate of desorption (Rd) can be expressed as:

$$Ra = Ka[O_3]_g([S] - [O_3]_s) \quad (9)$$

$$Rd = Kd[O_3]_s \quad (10)$$

where Ka is the adsorption rate constant (cm^3 $molecules^{-1}s^{-1}$), [S] is the total surface density of O_3 adsorption sites was taken as 5 x 10^{14} molecules cm^2 [*Dubowski et al.*, 2004; *Poschl et al.*, 2001]and Kd is the desorption rate constant(s^{-1}). At equilibrium adsorption rate constant (Ka) is equal to the desorption rate constant (Kd). This mechanism has been used by others to describe ozone's reaction with PAHs and soot. [*Kwamena et al.*, 2006; *Perraudin et al.*, 2007b].

Next we calculated a new γ based on this mechanism

$$\gamma = \frac{k_s[PAH]_0(1-f_t)}{\sqrt{\frac{RT}{2\pi M}}} \times \frac{[S]}{[O_3]_g + B} \quad (11)$$

where k_s is second order rate constant, f_t is the fraction of PAH or soot that has reacted with ozone at time t (f_t = abs(C=C)$_t$/abs(C=C)$_\infty$) in this case we take as f_t =0.5, which is half way through the initial reaction time period , and B is the ratio of Kd/Ka. We fitted equation (11) to our calculated γ data and obtain a k_s and B value. Figure 19 shows equation (11) fitted to our gamma data. Anthracene fit was poor at an ozone concentration of 40 ppm because of the oxidation rate of the C=O band was occurring at faster rate than 20 ppm and 80 ppm.. Table 2 presents the k_s and B values for all three

substances calculated using the equation (11). Note there is a fairly large uncertainty in the calculated values of $k_{s.}$ To improve upon this, additional experiments over a wide range of zone concentrations should be included in future studies.

Comparing our reaction rate constants we find that our results for our PAH calculations were in good agreement with other reported second order reaction rate constants. [*Kwamena et al.*, 2006] obtained surface reaction rates for anthracene in the range of $10^{-13} - 10^{-16}$ cm^2 $molecules^{-1}s^{-1}$,this range also incorporated the values reported here for both soot calculations. *Poschl et al.* [2001] investigated the surface reaction of benzo[a]pryene coating on a model soot particle with gaseous ozone and obtained a reaction rate constant of $2.6 \pm 0.8 \times 10^{-17}$ cm^2 $molecules^{-1}s^{-1}$, which is an order of a magnitude slower than our reaction rate constant. *Mmereki and Abbatt* [2004] also determined a rate constant of 2.6×10^{-17} cm^2 $molecules^{-1}s^{-1}$ for anthracene adsorbed at the air-water interface. Differences in our rates can be attributed to the amount of PAH reacted. We assume a uniform monolayer coverage when calculating our kinetics, when in fact our PAH may not have been completely evenly distributed on the crystal surface. A characterization of the coverage of PAH needs to be completed in order to determine a more accurate reaction rate constant. Possible errors associated with our soot reaction rate stem from the fact that we were unable to collect spectra of the soot throughout the oxidation process, the carbon (lampblack) had poor contact with the crystal, and the movement of the crystal to and from the hood, which could result in changes in coverage or islanding of soot particles on the sample plate.

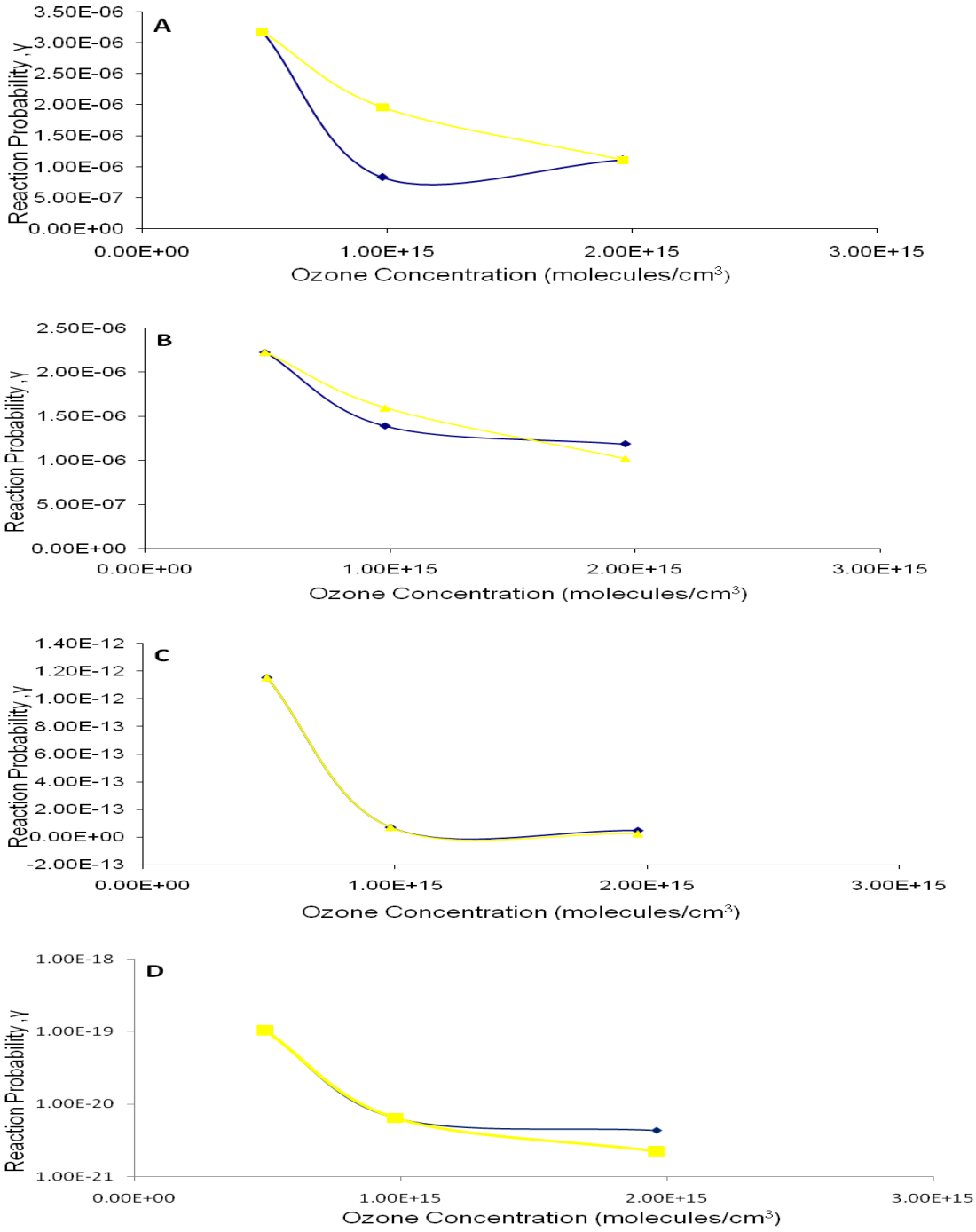

Figure 19. Calculated reaction probabilities for the oxidation of pyrene (a), anthracene (b), carbon (lampblack) geometric (c), and carbon (lampblack) BET (d). Blue line is initial reaction probabilities and yellow line is reaction probabilities when f_t=0.5.

Table 2. k_s and B values calculated using equation (11).

	Ks(cm^2 $moleclues^{-1}$ s^{-1})	B (molecules cm^{-3})
Pyrene	9.58E-16	7.51E+14
Anthracene	8.73E-16	3.03E+14
Carbon, Lampblack		
Geometric Area	7.71E-13S	-4.58E+14
BET Area	7.73E-13	-4.58E+14

3.3 Optical Measurement Results

Uv-visible spectra were collected to determine if the oxidation of PAHs by ozone changed their optical properties. Spectra of the two substances prior and after oxidation are presented in Figure 20. Anthracene absorbs more in the UV range of 190 nm- 380 nm after exposure to ozone. Pyrene in general absorbs more strongly in the UV range of 300 nm -330 nm when compared to Anthracene, in both oxidized and fresh cases. The UV-Visible Spectrophotometer max absorbance limit is 3.99 absorbance units, our 0.02 mg/ml solutions of pyrene hit this value multiply times in the UV range (300 nm -330 nm). Therefore, conclusions about how oxidation changes pyrene UV absorption were unable to be made, but changes in the visible absorption were observed.

In order to observe if there are any changes in the absorbance in the visible range of the spectrum, we had to zoom in on the tail end of the spectra graphed below in Figure 20, provided in Figure 21.

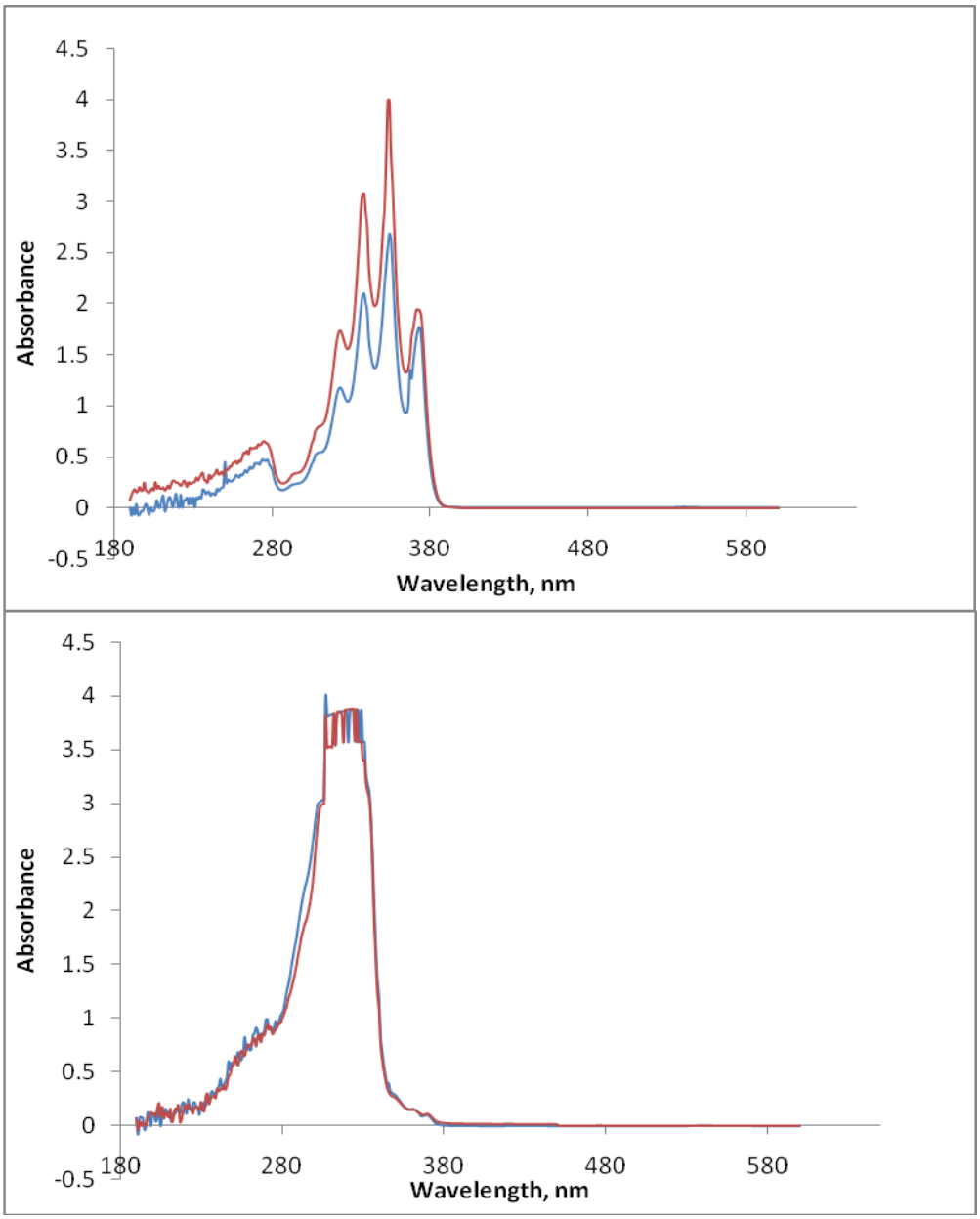

Figure 20. UV-visible spectra of anthracene (top) and pyrene (bottom) prior (blue) to and after 24 hours of oxidation (red) by 80 ppm of ozone.

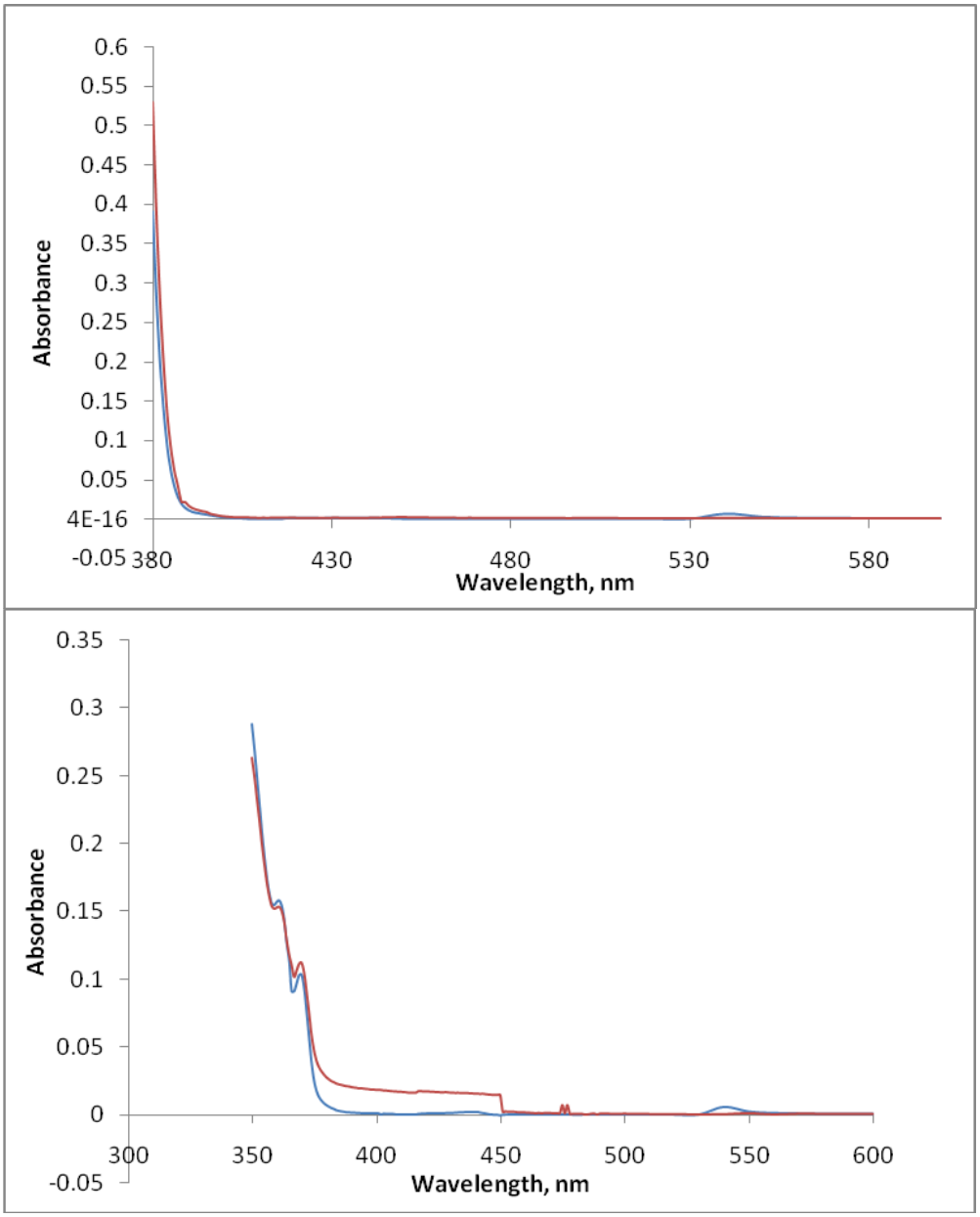

Figure 21. UV-visible spectra of anthracene (top) and pyrene (bottom) prior (blue) to and after 24 hours of oxidation (red) by 80 ppm of ozone zoomed in to 300 nm-600 nm.

From Figure 21, we can see that pyrene absorbs more in the visible range of 400 nm-450 nm after oxidation by ozone, while anthracene does not. In this figure we can also see a slight increase in the UV absorption of pyrene from 370nm-400nm. Similar results were observed by *Kwamena and Abbatt* [2008], where pyrene and anthracene were exposed to $NO_3/NO_2/N_2O_5$. In that study, it was shown that anthracene increased not only in the UV range of 300 nm-375 nm but the oxidized sample was also somewhat absorbing in the visible range of 400nm-500nm, which we did observe here. *Kwamena and Abbatt* [2008] also observed similar results for pyrene. Our result combined with *Kwamena and Abbatt's* [2008] show that as PAHs interact with trace gases in the atmosphere they have the potential to alter their optical properties. These alterations can lead to more absorbing particles, which act to warm the surrounding atmosphere. Changes in the scattering and absorption properties of these aerosols can lead to changes in the radiative balance.

3.4 Hygroscopicity Results

In order to determine if the ESEM was functioning correctly and our temperature measurements were accurate, calibration experiments were conducted routinely. Sodium chloride (NaCl) is a well-characterized salt with a DRH of 75%. This salt was chosen as the calibration salt for these experiments. Figure 22 is an example of a NaCl particle deliquescing. Using our method described above we routinely reproduced a DRH of ~75%, which is illustrated in Figure 23.

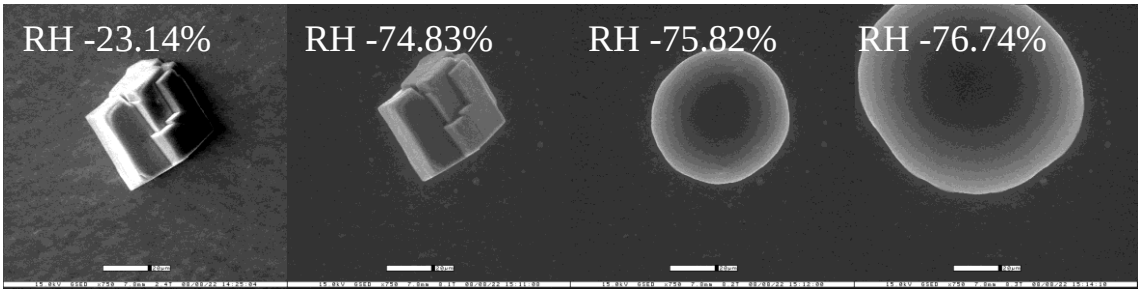

Figure 22. ESEM images of NaCl particle (~ 60 µm) during a water up-take experiment.

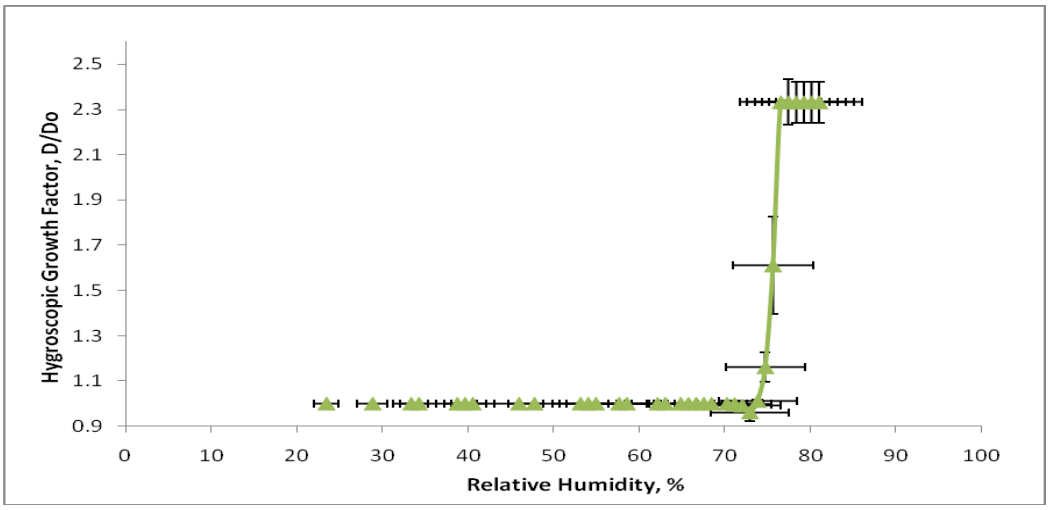

Figure 23. Average hygroscopic growth factor as a function of relative humidity for a NaCl particle of ~60µm.

After the initial NaCl calibration, uptake experiments were conducted on individual particle samples composed of carbon (lampblack), pyrene, and anthracene. Figure 24 contains ESEM images collected during experimental runs for each substance (carbon (lampblack), pyrene, and anthracene). For each compound the top row shows an experiment conducted on a fresh sample and the bottom row shows a representative ESEM experiment conducted on an oxidized sample. Water uptake curves were plotted

for each substance, seen in Figure 25. The data collected at each RH in the figure is the average based on three independent experiments on three individual particles. The average D/Do for each substance, fresh and oxidized, was plotted with an average NaCl curve. From the curves it is clear that no water uptake was occurring, exposed particles remained the same size from ~20% to ~100%.

Prior to ozone exposure, none of these particles exhibited the uptake behavior of a deliquescent compound. In all cases the fresh materials were highly non-hydroscopic. As can be seen in Figure 24, oxidation did not cause observable changes in the water uptake.

Others have observed oxidized soot particles activating at lower superstations than fresh soot using different techniques than the one explored here, such as a cloud condensation nucleus chamber and light reflectometry [*Kotzick et al.,* 1997; *Zuberi et al.*, 2005]. *Zuberi et al*. [2005]observed water uptake on aged soot exposed to $OH/O_3/H_20/UV$ at 2 ± 2% supersaturation using Light Reflectometry (LR). LR is a technique that measures the intensity of reflected light from a laser beam focused onto a sample. However, as shown in Figure 26 at relative humidities as high as 105%, in this experiment, we observed no signs of water uptake by the particle properties for any of the substances.

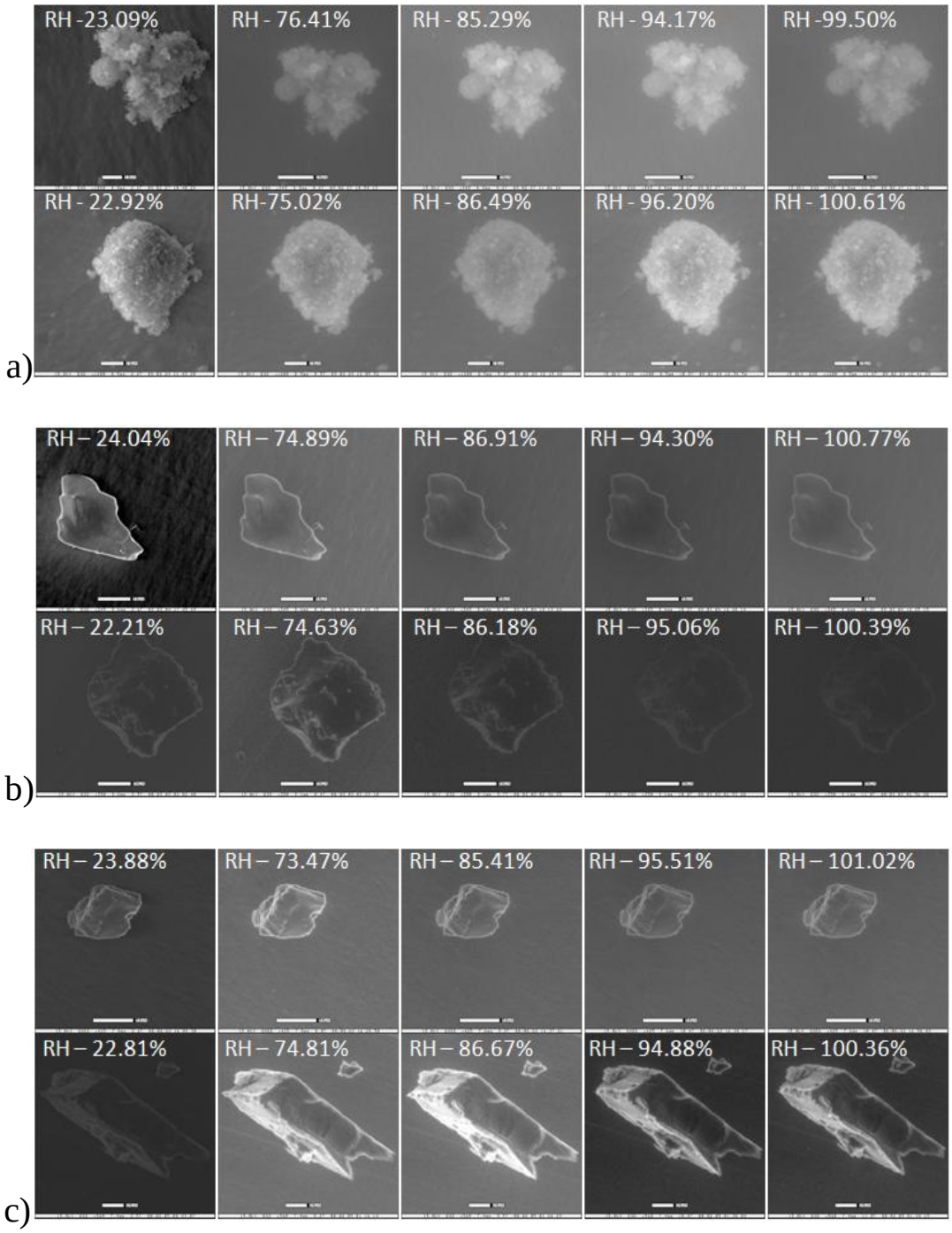

Figure 24. ESEM images obtained during water uptake experiments. Particles in **a** are carbon (lampblack) fresh (top) and oxidized (bottom), **b** are pyrene particles fresh (top) and oxidized (bottom), and **c** are anthracene particles un-oxidized(top) and oxidized(bottom). Oxidized particles were exposed to 80 ppm of ozone for 24 hours.

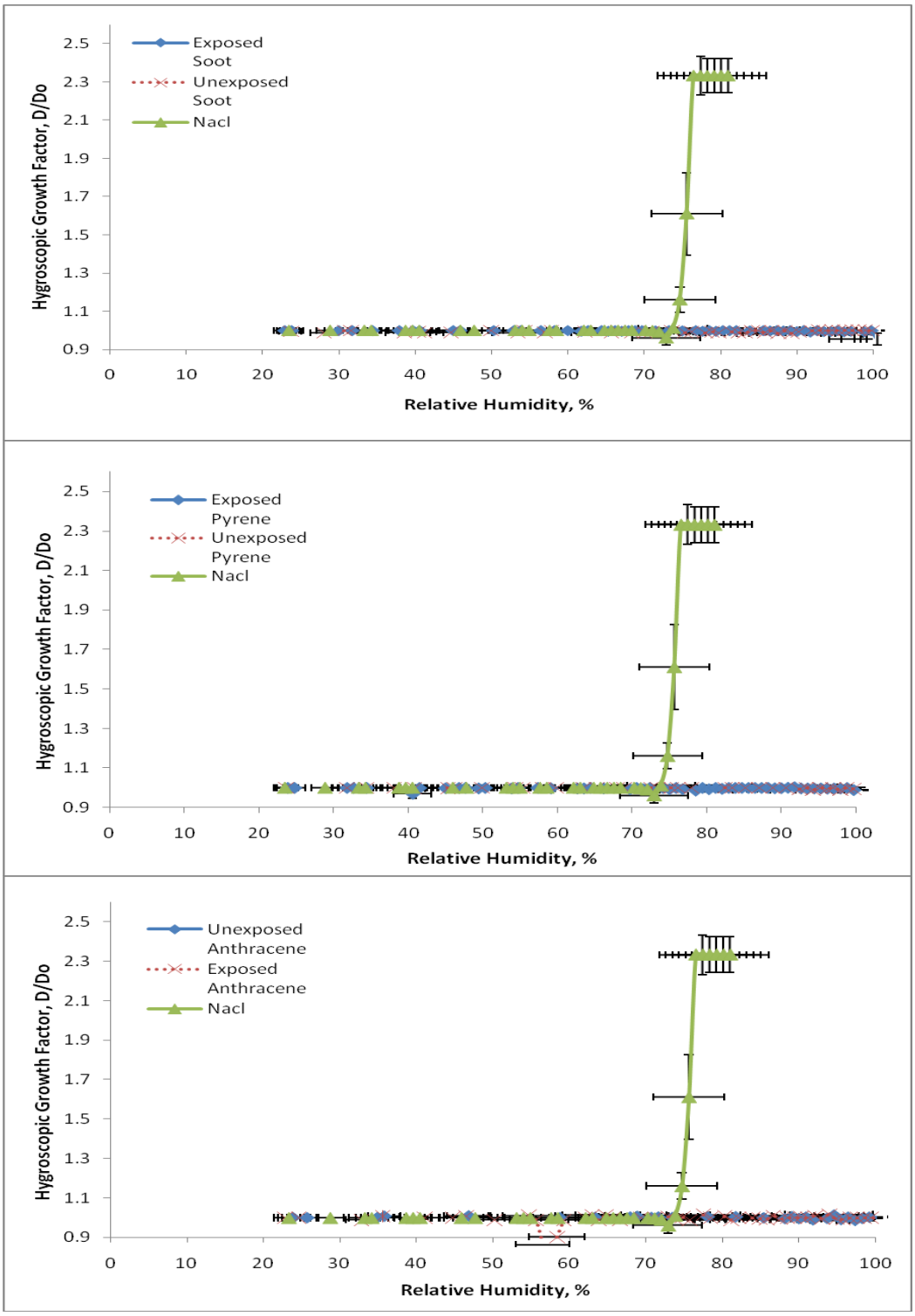

Figure 25. Hygroscopic growth factor as a function of humidity for sodium chloride, soot (carbon,lampblack), pyrene, and anthracene.

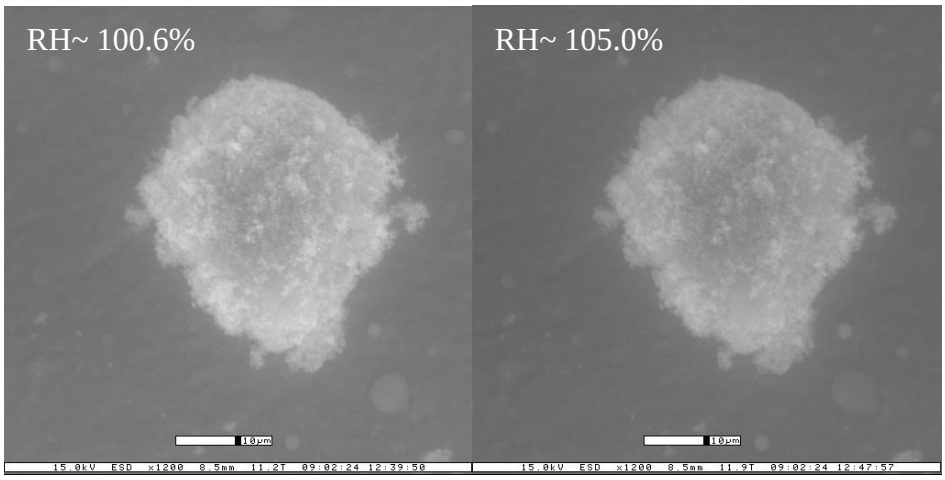

Figure 26. ESEM images of oxidized soot particles above 100% RH. Water condensation occurred on the stage but not the particle.

In order to determine if we were missing any potential water uptake we conducted two additional experiments. The first thought was we had not oxidized the surface of the particles, therefore we exposed a sample to a high amount of ozone >20,000 ppm. We were still unable to observe any water uptake. Secondly, we took a sample to an RH of 105% to see if any water uptake occurred past 100%. We saw condensation occurring on the stage at 100% but again no water uptake was observed on the particle. Figure 26 illustrates this for an oxidized soot particle exposed to 80 ppm of ozone for 24 hours. After verifying our results using these two test we concluded that oxidation of PAHs or carbon (lampblack) does not alter the deliquesce behavior of our samples, as observed by the ESEM. Within the uncertainty of these experiments, neither fresh nor oxidized samples show any indication of water uptake over the range of relative humidities examined in these experiments.

The ESEM used in this study is a robust technique for monitoring physical changes in single particles as small as 0.5 microns in size. However, a caveat of the ESEM method is that changes occurring at particle's surface are below the limit of detection. Suppose water was forming one monolayer at a time on the surface of a particle. Based on the size of a water molecule (2.75 A°) and the limit of detection of the ESEM (0.5 microns), we estimate that 1818 monolayers of water would need to form for us to be detectable with the ESEM.

Popovicheva et al. [2008b] suggested a concept of quantification of the water uptake by soot particles, in which two mechanisms of water/soot interaction occur, bulk dissolution into soot-water-soluble coverage (absorption mechanism) and water molecule adsorption on surface active sites (adsorption mechanism). While we cannot rule out the possibility that some water is adsorbed to the particles, the amount of water is below the detection limit of our ESEM measurements.

3.5 Ice Efficiency Results

Oxidized soot froze at an average temperature of -22.8°C, while fresh soot froze at an average temperature of-25.6°C. A total of 125 freezing events were obtained for oxidized soot. All of the freezing events for fresh and oxidized carbon (lampblack) are presented in Figure 27.

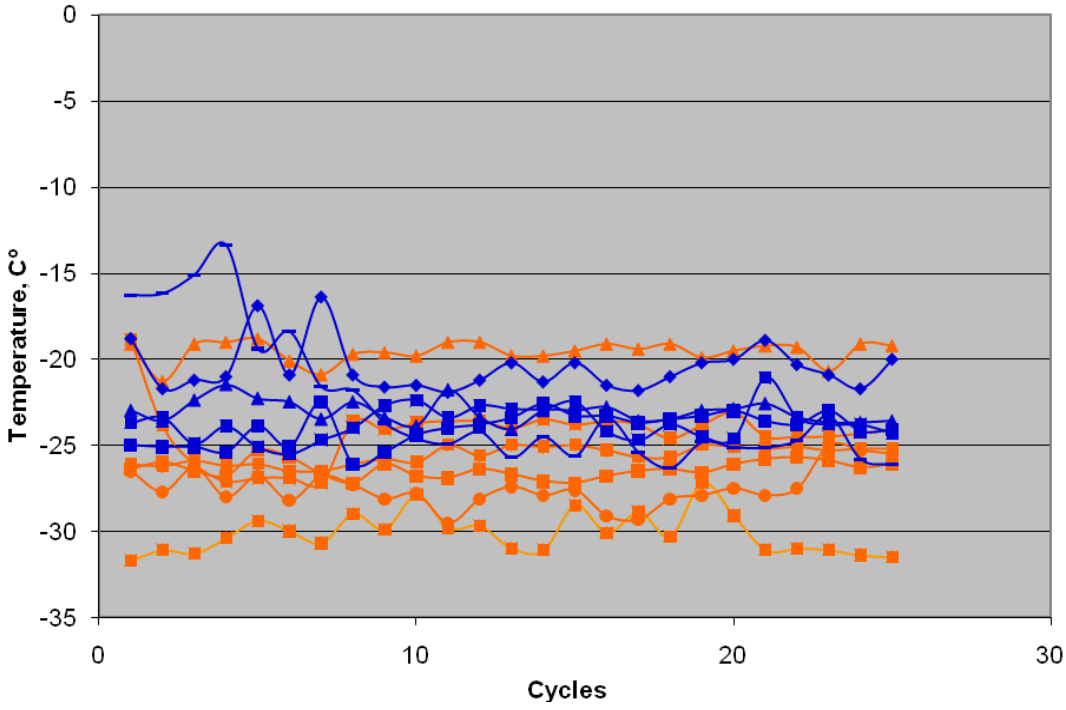

Figure 27. Freezing event temperatures for fresh (orange) and oxidized soot (blue).

The two means of the fresh and oxidized soot were compared to determine if they were statistically significantly different at a confidence level of 99% using the equation:

$$\bar{x}_1 - \bar{x}_2 = \pm t s_{pooled} \sqrt{\frac{N_1 + N_2}{N_1 N_2}} \tag{12}$$

where $\bar{x}_1$ = -22.8°C , $\bar{x}_2$ =-25.6°C , s_{pooled} is the pooled standard deviation of both data sets of 3.3°C , $N_1$is the number of observations for oxidized soot 125,N_2 is the number of observations of fresh soot 150, and t at 99% is 3.29. s_{pooled} was calculated by taking each observation and subtracting it from the mean, each value obtained was squared and

summed. This summation was then divided by the total number of observations in both data sets minus the number of data sets. The square root of the obtain value is s_{pooled}. The right side of the equation equals 1.31 which is less then $\bar{x}_1 - \bar{x}_2$ (2.8), therefore there was a significant difference between the two means.

Unlike the ESEM, here we were able to observe a clear difference in the characteristic behavior of fresh and oxidized samples. Specifically, we observed an increase in the temperature at which freezing occurs in the oxidized samples. These results show that we indeed changed the composition of our soot particles and the atmospheric conditions under which droplets with IN of oxidized soot can initiate freezing. Even with our extreme O_3 concentration of 80 ppm, it is reasonable to assume that we would still see an increase on a smaller scale in the freezing temperature of oxidized soot at more reasonably atmospheric ozone concentrations (~30 ppb - 40 ppb). *Dymarska et al* [2006]found that oxidation of Lamp Black did not change the IN ability significantly, however they observed ice nucleation by deposition not contact or immersion as was done here.

The increase in the freezing temperature can possibly be explained by a composition change of the aerosol, an increase in the surface area and/or a change in the freezing mechanism. A compositional change can affect the particles affinity for water. In our case we attributed the formation of the C=O band, due to oxidation, as a location on which water could attach. This formation changed the hygroscopicity of our substances from hydrophobic to hydrophilic. The hygroscopicity change allowed the soot particle to disperse into the droplet. Unlike the oxidized soot, fresh soot is

hydrophobic and previous experiments showed that the soot particle stayed in contact with the surface of the droplet; therefore freezing by the mechanism of contact freezing. Figure 28 illustrates the difference in the location of the IN for oxidized and fresh soot.

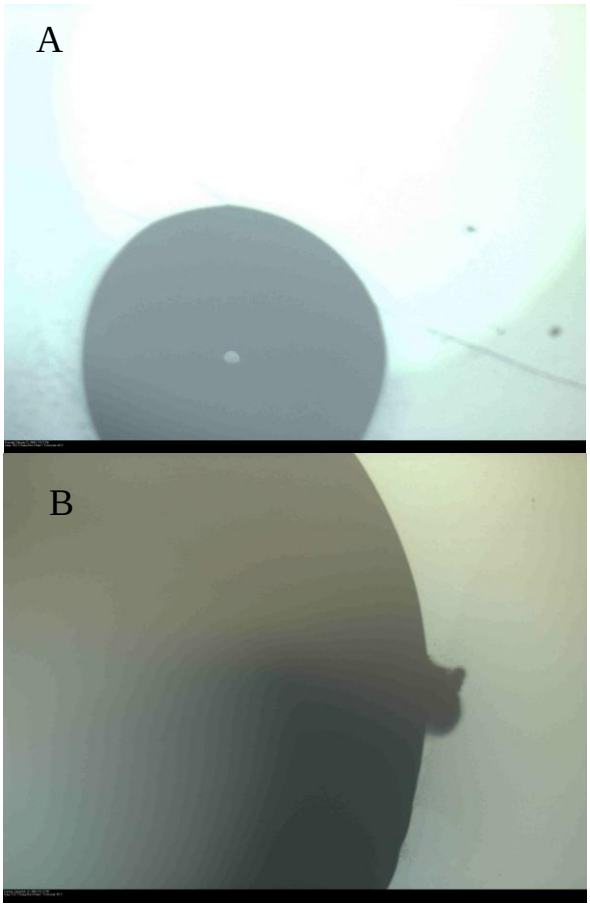

Figure 28. Images of ultra pure water droplets that have been inserted with IN. Image A is a droplet that contains oxidized soot. The IN has entered the droplet and turned it dark; making it appear it has gone in solution. Image B is a droplet in contact with a fresh soot particle, the soot remains on the outer edge of the droplet for the entire experiment.

This dispersion of the oxidized soot possibly increased the surface area of the soot particle that was in contact with the droplet surface, therefore allowing the droplet to freeze at a warmer temperature. How the particle is in contact with the droplet can govern which mechanism the particle freezes by. The hygroscopicity change may have allowed for our soot particle to be placed in the droplet, allowing for immersion freezing. Since our droplet is so dark it hard to determine the actually location of the soot particle. Immersion freezing is expected to occur at lower temperatures then contact freezing, but in previous experiments immersion freezing was not observed due to the extreme hydrophobic nature of the fresh carbon (lampblack). *Fornea et al*.[2009] observed warmer freezing temperatures for contact freezing of volcanic ash then for immersion freezing. An average contact freezing temperature of -11.2 °C ± 1.0 °C and an average immersion freezing temperature of -18.3 °C ± 2.0 °C were observed for the volcanic ash. *Durant and Shaw* [2005]observe similar results with regard to contact versus immersion freezing, a 4 ºC to 5ºC difference. We clearly observed an increase in freezing temperature due to a compositional change in the soot surface.

4. ATMOSPHERIC IMPLICATIONS

Oxidation of PAHs and carbon (lampblack) by ozone leads to the formation of C=O band, which is characteristic of carboxylic acids. Freshly emitted is soot is hydrophobic, but oxidation can change soot into a hydrophilic substance [*Rudich*, 2003].Two possible mechanisms were explored in order to gain a better understanding of how oxidation could possibly affect CCN activity of PAHs and soot particles. In case A, we believed that only the surfaces of our samples were transformed, leading to a surface layer that resembles the structure of oxalic acid. As mention before, *Propovicheva et al*. [2008b] suggested a concept of quantification of the water uptake by soot particles, in which two mechanisms of water/soot interaction occur, bulk dissolution into soot-water-soluble coverage (absorption mechanism) and water molecule adsorption on surface active sites (adsorption mechanism). The latter of the two is what we think occurred in this experiment; we changed the surface of the particles which allowed water to attach to the active sites possibly leading to a formation of a monolayer of water. We created wettable particles, in which water could attached and form a coating. This coating of water could enable the particle to activate and grow into a cloud droplet. This mechanism would only be observed by the ice nucleation method, which is what we observed in our study. Case B, we imagine a spherical shape insoluble soot particle with a radius of 100 nm. Part of this soot particle is converted in to soluble components resembling, for example, oxalic acid. This conversion would allow the droplet to activate at a lower superstation and grow similar to a pure dilute droplet of oxalic acid. This

mechanism would be observed by both the ESEM and the ice nucleation experiments, but as discussed above we did not observe any water uptake using the ESEM method; therefore we believe case A is the mechanism occurring here.

We applied Köhler theory to calculate the superstation needed to activate dilute solution droplets of oxalic acid, ammonium sulfate, and pure water. Here we chose, oxalic acid, which is one of the most abundant dicarboxylic acids in the atmosphere [*Giebl et al.*, 2002]to hypothetically represent the soluble oxidized product which could form as a result of the reactions our samples underwent with ozone. For comparison ammonium sulfate was used for a representative salt. In case B, we applied a modified Köhler theory, in which a droplet contained an insoluble core (soot), was applied to calculate the superstations needed to activate different droplets containing 0.1% mass conversion and 10% mass conversion.

The water vapor pressure at the surface of an aqueous solution droplet of a certain radius, at equilibrium conditions, is determined by two opposing effects, the Kelvin effect and the Raoult effect. The Kelvin effect, known as the curvature effect, increases the equilibrium vapor pressure. Conversely, the Raoult effect, also known as the solution effect, works to decrease the equilibrium vapor pressure. The Köhler equation is a combination of both of these effects, for dilute solutions approximation of the saturation ratio adjacent to a solution droplet is:

$$\frac{e_s'(r)}{e_s(\infty)} = 1 + \frac{a}{r} - \frac{b}{r^3} \qquad (13)$$

where $a = 2\sigma' / \rho_l R_v T$ and $b = 3im_v M / 4\pi\rho_l m_s$, r is the radius of the droplet, σ' surface tension of water, ρ_l is the density of water, R_v is the gas constant of water vapor, T is the temperature (20 °C), i is the Van't Hoff factor , M is the mass of solute, m_s is the molecular weight of the solute, and m_v is the molecular mass of water. For dilute solutions a and b can be further simplified to $a = 3.3 \times 10^{-5} / T$ and $b = 4.3iM / m_s$. For the solutions of oxalic acid (i=1.1) and ammonium sulfate (i=3).

For a droplet containing an insoluble core a modified version of Kohler Theory is given by equation, which has been adapted from *Pruppacher and Klett* [1997].

$$\frac{e_s'(r)}{e_s(\infty)} = exp^{\frac{2M_W\sigma'}{RTa\rho_W} - \frac{i\phi_s\epsilon_m M_W \rho_n r_n^3}{M_s\rho_W(a^3 - r_n^3)}} \quad (14)$$

where M_w is the molecular mass of water, a is the radius of the droplet, ρ_w is the density of water, r_n is the radius of insoluble core, is the ϕ-osmotic coefficient(1.3), ε_m is the mass fraction, ρ_n- density of the core, and M_s the molecular mass of the solute (oxalic acid). Köhler curves can be obtained, as seen in Figure 29. Therefore, if our samples are being transformed into surfaces that resemble the structure of oxalic acid, it is reasonable to assume that after oxidation the PAH and soot particles would activate at lower supersaturations, improving their CCN abilities.

Similar conclusions on the CCN behavior of organic aerosols have been reported [*Kreidenweis et al.*, 2006; *Petters and Kreidenweis*, 2007; 2008]. Future work will try to differentiate between the two cases using a CCN counter, as well as confirm our findings that oxidation by ozone not only improves ice efficiency but CCN abilities as well.

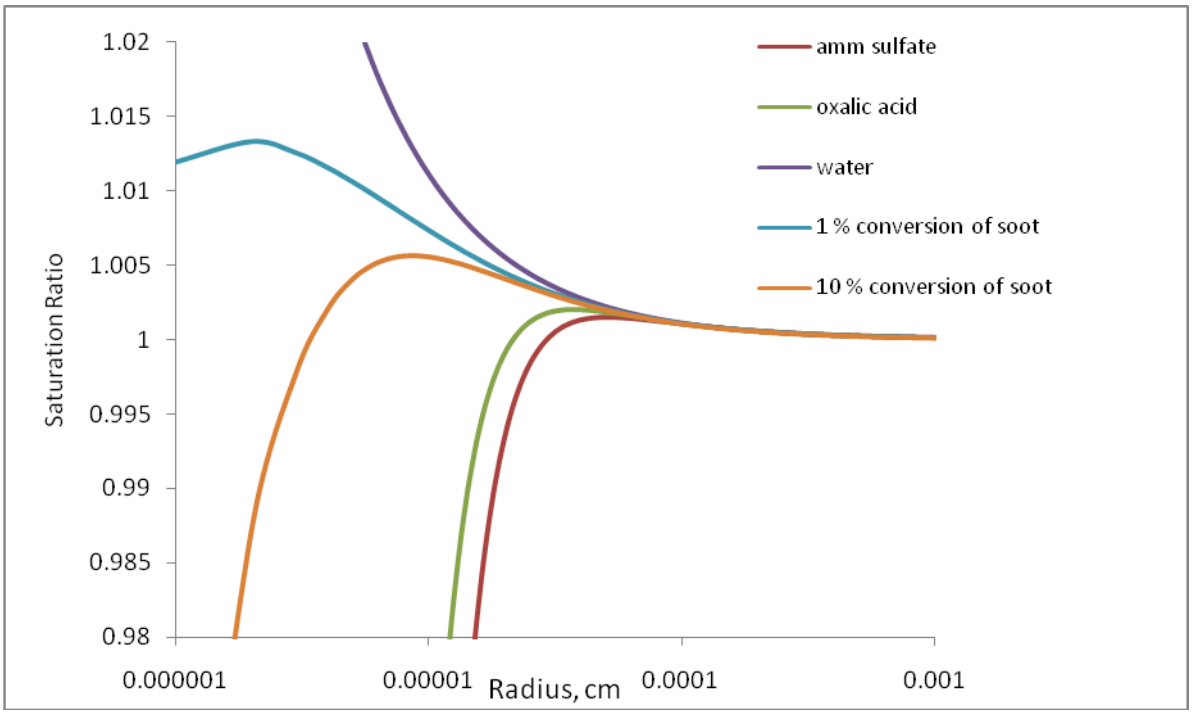

Figure 29. Equilibrium saturation ratio of solution droplets formed on soot with 1% and 10% conversion, ammonium sulfate, oxalic acid and pure water condensation nucleus of mass 10^{-16} g.

5. CONCLUSIONS

In this study, we identified the chemical changes which occur at the surface of carbon (lampblack) and PAHs as they react with gas phase ozone. These chemical properties are linked to important physical characteristics of the aerosols including optical properties, ability to take up water, and ice nucleation efficiency. We showed that oxidation by ozone of these particles changes their optical properties as well as their hygroscopic properties improving their ability to act as IN and possibly their CCN ability.

Employing the FTIR-HATR, allowed us to observe the chemical bonds in our substances and to track how exposure to ozone changed certain bonds over time. Our results indicated a formation of a C=O band at the surface for all three substances studied here, carbon (lampblack), pyrene, and anthracene. The C=O band is characteristic of aldehydes and carboxylic acids [*Skoog et al.*, 1998]. The addition of these functional groups provides a surface on which water can attach, enhancing the substances ability to uptake water and/or act as more efficient IN. Our kinetic calculations indicate that the reactions studied here proceeds by a Langmuir-Hinshelwood mechanism. We obtained second order rate constants of 9.58×10^{-16} cm^2 $molecules^{-1}$ s^{-1}, 8.73×10^{-16} cm^2 $molecules^{-1}$ s^{-1} for pyrene and anthracene, respectively. For carbon (lampblack), we calculated rate constants for the soot based on the both its geometric area and its BET area, 7.71×10^{-13} cm^2 $molecules^{-1}$ s^{-1} and 7.73×10^{-13} cm^2 $molecules^{-1}$ s^{-1}, respectively. Unlike the rate constants for soot, the reaction probabilities

for the geometric area and BET area varied greatly. Reported values were on the order of 10^{-14} for the geometric area and 10^{-21} for the BET area. While our PAH reaction rate constants agree with other reported rate constants, our soot rates are larger than those reported by others. The inability to collect spectra of the soot throughout the oxidation process and the inconsistent nature of the coverage on the crystal led to possible errors in our soot kinetic calculations.

Measurements of the optical properties were made for the PAHs to determine if the reaction with ozone increased the absorbance of these particles in the UV and visible ranges. We observed an increase in the UV absorbance for anthracene, but not in the visible while pyrene showed an increase in absorption in the visible range. These increases can lead to changes in the absorption properties of these aerosols and the total aerosol extinction, which can lead to changes in the Earth's radiative budget.

Water uptake was examined using the ESEM technique. This technique allowed us to control the RH samples were exposed to. Oxidized and fresh samples were studied to determine if oxidation led to improve water uptake ability. Due to the limitations in the ESEM detection limit we did not observe any water uptake changes after oxidation.

IN efficiency was determined by observing the freezing events of droplets inserted with oxidized soot. This technique allowed us to determine between contact and immersion freezing, which have been shown to occur at different temperatures [*Durant and Shaw*, 2005; *Fornea et al.*, 2009]. We observed an average freezing temperature of -22.8°C for oxidized soot, which is warmer then the fresh soot freezing at an average temperature of -25.6°C [*Fornea et al.*, 2009]. It was found that these

averages were significantly different at a confidence level of 99%, showing that oxidation does improve the ice nucleation efficiency of carbon (lampblack).

Köhler theory was applied in order to gain a better understanding of how the oxidation of PAHS and carbon (lampblack) by ozone could affect the CCN activity of these particles. The oxidation of our particles leads to the formation of carboxylic acids on the surface of our substances. For comparison, the CCN activity of oxalic acid a representative dicarboxylic acid was included. It was shown that a solution droplet containing oxalic acid activates at a lower supersaturation then a solution droplet containing pyrene. Therefore we concluded that if we are changing the surfaces of our substances to something that resembles the structure of oxalic acid, it is reasonable to assume that the particle after oxidation would activate a lower supersaturation. Alternatively, if we are creating wettable particles, in which a monolayer of water can form, there will also be a change in CCN activity relative to the initial hydrophobic particles. Future work will include direct CCN measurements on fresh and oxidized species to directly assess the impacts of chemical aging.

Our results here indicate that the oxidation of soot and the PAHS by ozone have potentially imported impacts on how these particles interact with the microphysical properties of clouds. Along with how these particles change their CCN and IN ability changes in their optical properties have implications for the radiative budget. Knowing how the aging of these particles affect them chemically, gives us a better understanding on how they physical change. These physical changes have implications for atmospheric process, which affects the Earth’s climate.

REFERENCES

Al-Hosney, H. A., and V. H. Grassian (2005), Water, sulfur dioxide and nitric acid adsorption on calcium carbonate: A transmission and ATR-FTIR study, *Physical Chemistry Chemical Physics*, *7*(6), 1266-1276.

Bertram, A. K., D. D. Patterson, and J. J. Sloan (1996), Mechanisms and temperatures for the freezing of sulfuric acid aerosols measured by FTIR extinction spectroscopy, *Journal of Physical Chemistry*, *100*(6), 2376-2383.

Calvert, J. G. (2002), *The Mechanisms of Atmospheric Oxidation of Aromatic Hydrocarbons*, Oxford University Press, Oxford.

Chughtai, A. R., J. A. Jassim, J. H. Peterson, D. H. Stedman, and D. M. Smith (1991), Spectroscopic and solubility characteristics of oxidized soots, *Aerosol Science and Technology*, *15*(2), 112-126.

Chughtai, A. R., G. R. Williams, M. M. O. Atteya, N. J. Miller, and D. M. Smith (1999), Carbonaceous particle hydration, *Atmospheric Environment*, *33*(17), 2679-2687.

Decesari, S., M. C. Facchini, E. Matta, M. Mircea, S. Fuzzi, et al. (2002), Water soluble organic compounds formed by oxidation of soot, *Atmospheric Environment*, *36*(11), 1827-1832.

Dubowski, Y., J. Vieceli, D. J. Tobias, A. Gomez, A. Lin, et al. (2004), Interaction of gas-phase ozone at 296 K with unsaturated self-assembled monolayers: A new look at an old system, *Journal of Physical Chemistry A*, *108*(47), 10473-10485.

Durant, A. J., and R. A. Shaw (2005), Evaporation freezing by contact nucleation inside-out, *Geophys. Res. Lett.*, *32*, 1-4.

Dymarska, M., B. J. Murray, L. Sun, M. L. Eastwood, D. A. Knopf, et al. (2006), Deposition ice nucleation on soot at temperatures relevant for the lower troposphere, *J. Geophys. Res.*, *111*, 1-9.

Ebert, M., M. Inerle-Hof, and S. Weinbruch (2002), Environmental scanning electron microscopy as a new technique to determine the hygroscopic behavior of individual aerosol particles, *Atmospheric Environment*, *36*(39-40), 5909-5916.

Facchini, M. C., S. Decesari, M. Mircea, S. Fuzzi, and G. Loglio (2000), Surface tension of atmospheric wet aerosol and cloud/fog droplets in relation to their organic carbon content and chemical composition, *Atmospheric Environment*, *34*(28), 4853-4857.

Finlayson-Pitts, B. J., and J. N. Pitts (1986), *Atmospheric Chemistry: Fundamentals and Experimental Techniques*, Wiley, New York.

Finlayson-Pitts, B. J., and J. N. Pitts (2000), *Chemistry of the Upper and Lower Atmosphere: Theory, Experiments and Applications*, Academic Press, San Diego, California.

Fornea, A. P., S. D. Brooks, B. Dooley, and A. Saha (2009), Heterogeneous freezing of ice on atmospheric aerosols containing ash, soot, and soil, *Journal of Geophysical Research-Atmospheres*, Accepted.

Giebl, H., A. Berner, G. Reischl, H. Puxbaum, A. Kasper-Giebl, et al. (2002), CCN activation of oxalic and malonic acid test aerosols with the University of Vienna cloud condensation nuclei counter, *J. Aerosol. Sci.*, *33*(12), 1623-1634.

Harrick, N. J. (1967), *Internal Reflection Spectroscopy*, Harrick Scientific Corp., Ossining, New York.

Hiranuma, N., S. D. Brooks, B. W. Auvermann, and R. Littleton (2008), Using environmental scanning electron microscopy to determine the hygroscopic properties of agricultural aerosols, *Atmospheric Environment*, *42*(9), 1983-1994.

Hung, H. M., Y. Katrib, and S. T. Martin (2005), Products and mechanisms of the reaction of oleic acid with ozone and nitrate radical, *Journal of Physical Chemistry A*, *109*(20), 4517-4530.

Hunter, R. J. (1993), *Introduction to Modern Colloid Science*, 1st ed., Oxford University Press, Oxford.

IPCC (2007), *Climate Change 2007: The Physical Science Basis. Summary for Policy Makers. Contribution of Working group 1 to the Fourth Assessment Report of the Intergovernmental Panel for Climate Change*, 21 pp., IPCC Secretariat, Geneva.

Kotzick, R., U. Panne, and R. Niessner (1997), Changes in condensation properties of ultrafine carbon particles subjected to oxidation by ozone, *J. Aerosol. Sci.*, *28*(5), 725-735.

Kotzick, R., and R. Niessner (1999), The effects of aging processes on critical supersaturation ratios of ultrafine carbon aerosols, *Atmospheric Environment*, *33*(17), 2669-2677.

Kreidenweis, S. M., M. D. Petters, and P. J. DeMott (2006), Deliquescence-controlled activation of organic aerosols, *Geophys. Res. Lett.*, *33*, 1-4.

Krueger, B. J., V. H. Grassian, A. Laskin, and J. P. Cowin (2003), The transformation of solid atmospheric particles into liquid droplets through heterogeneous chemistry: Laboratory insights into the processing of calcium containing mineral dust aerosol in the troposphere, *Geophys. Res. Lett.*, *30*(3), 41-48.

Kwamena, N. O. A., M. E. Earp, C. J. Young, and J. P. D. Abbatt (2006), Kinetic and product yield study of the heterogeneous gas-surface reaction of anthracene and ozone, *Journal of Physical Chemistry A*, *110*(10), 3638-3646.

Kwamena, N. O. A., and J. P. D. Abbatt (2008), Heterogeneous nitration reactions of polycyclic aromatic hydrocarbons and n-hexane soot by exposure to $NO_3/NO_2/N_2O_5$, *Atmospheric Environment*, *42*(35), 8309-8314.

Kwok, E. S. C., W. P. Harger, J. Arey, and R. Atkinson (1994), Reactions of gas-phase phenanthrene under simulated atmospheric conditions, *Environmental Science & Technology*, *28*(3), 521-527.

Kwok, E. S. C., R. Atkinson, and J. Arey (1997), Kinetics of the gas-phase reactions of indan, indene, fluorene, and 9,10-dihydroanthracene with OH radicals, NO_3 radicals, and O_3, *International Journal of Chemical Kinetics*, *29*(4), 299-309.

Lary, D. J., D. E. Shallcross, and R. Toumi (1999), Carbonaceous aerosols and their potential role in atmospheric chemistry, *Journal of Geophysical Research-Atmospheres*, *104*(D13), 15929-15940.

Lide, D. R. (Ed.) (2008), *CRC Handbook of Chemistry and Physics*, 89th edition,CRC Press, Boca Raton, Florida.

Liousse, C., J. E. Penner, C. Chuang, J. J. Walton, H. Eddleman, et al. (1996), A global three-dimensional model study of carbonaceous aerosols, *Journal of Geophysical Research-Atmospheres*, *101*(D14), 19411-19432.

Lynch, D. K. (2002), *Cirrus*, Oxford University Press, New York.

McCabe, J., and J. P. D. Abbatt (2009), Heterogeneous loss of gas-phase ozone on n-hexane soot surfaces: Similar kinetics to loss on other chemically unsaturated solid surfaces, *Journal of Physical Chemistry C*, *113*(6), 2120-2127
.

Mmereki, B. T., and D. J. Donaldson (2004), Direct observation of the kinetics of an atmospherically important reaction at the air-water interface, *The Journal of Physical Chemistry A*, *107*(50), 11038-11042.

Onasch, T. B., R. L. Siefert, S. D. Brooks, A. J. Prenni, B. Murray, et al. (1999), Infrared spectroscopic study of the deliquescence and efflorescence of ammonium sulfate

aerosol as a function of temperature, *Journal of Geophysical Research-Atmospheres*, *104*(D17), 21317-21326.

Penner, J. E., H. Eddleman, and T. Novakov (1993), Towards the development of a global inventory for black carbon emissions, *Atmospheric Environment Part A-General Topics*, *27*(8), 1277-1295.

Perraudin, E., H. Budzinski, and E. Villenave (2007a), Identification and quantification of ozonation products of anthracene and phenanthrene adsorbed on silica particles, *Atmospheric Environment*, *41*(28), 6005-6017.

Perraudin, E., H. Budzinski, and E. Villenave (2007b), Kinetic study of the reactions of ozone with polycyclic aromatic hydrocarbons adsorbed on atmospheric model particles, *Journal of Atmospheric Chemistry*, *56*(1), 57-82
.

Petters, M. D., and S. M. Kreidenweis (2007), A single parameter representation of hygroscopic growth and cloud condensation nucleus activity, *Atmos. Chem. Phys.*, *7*(8), 1961-1971.

Petters, M. D., and S. M. Kreidenweis (2008), A single parameter representation of hygroscopic growth and cloud condensation nucleus activity - Part 2: Including solubility, *Atmos. Chem. Phys.*, *8*(20), 6273-6279.

Popovicheva, O., E. Kireeva, N. Persiantseva, T. Khokhlova, N. Shonija, et al. (2008a), Effect of soot on immersion freezing of water and possible atmospheric implications, *Atmospheric Research*, *90*(2-4), 326-337.

Popovicheva, O. B., N. M. Persiantseva, V. Tishkova, N. K. Shonija, and N. A. Zubareva (2008b), Quantification of water uptake by soot particles, *Environmental Research Letters*, *3*(2), 1-12.

Poschl, U., T. Letzel, C. Schauer, and R. Niessner (2001), Interaction of ozone and water vapor with spark discharge soot aerosol particles coated with benzo[a]pyrene: O_3 and H_2O adsorption, benzo[a]pyrene degradation, and atmospheric implications, *The Journal of Physical Chemistry A*, *105*(16), 4029-4041.

Poschl, U. (2005), Atmospheric aerosols: Composition, transformation, climate and health effects, *Angew. Chem.-Int. Edit.*, *44*(46), 7520-7540.

Pruppacher, H. R., and J. D. Klett (1997), *The Microphysics of Clouds and Precipitation*,2nd revised and enlarged edition, Kluwer Academic Publishers, Dordrecht, The Netherlands.

Rogers, D. C. (1988), Development of a continuous flow thermal gradient diffusion chamber for ice nucleation studies, *Atmospheric Research*, *22*(22), 149-181.

Rosenfeld, D. (2000), Suppression of rain and snow by urban and industrial air pollution, *Science*, *287*(5459), 1793-1796.

Rudich, Y. (2003), Laboratory perspectives on the chemical transformations of organic matter in atmospheric particles, *Chemical Reviews*, *103*(12), 5097-5124.

Seinfeld, J. H., and S. N. Pandis (2006), *Atmospheric Chemistry and Physics: From Air Pollution to Climate Change*, 2nd ed., J. Wiley, Hoboken, New Jersey.

Skoog, D. A., F. J. Holler, and T. A. Nieman (1998), *Principles of Instrumental Analysis*, 5th ed., 1 v. (various pagings) pp.,Harcourt Brace College Publishers, Philadelphia

Twomey, S., Piepgrass, M. and Wolfe, T.L. (1984), An assessment of the impact of pollution on the global cloud albedo, *Tellus*, *36B*, 356-366.

Vali, G. (1985), Nucleation terminology, *J. Aerosol. Sci.*, *16*(6), 575–576.

Wallace, J. M., and P. V. Hobbs (2006), *Atmospheric Science: An Introductory Survey*, 2nd ed., Elsevier Academic Press, Amsterdam.

Weingartner, E., H. Burtscher, and U. Baltensperger (1997), Hygroscopic properties of carbon and diesel soot particles, *Atmospheric Environment*, *31*(15), 2311-2327.

Zuberi, B., K. S. Johnson, G. K. Aleks, L. T. Molina, M. J. Molina, et al. (2005), Hydrophilic properties of aged soot, *Geophys. Res. Lett.*, *32*, 1-4.

APPENDIX A

The depth of penetration depends on the wavelength of light, the refractive index of the crystal, incident angle of the IR beam, and refractive index of the substance in contact with the crystal. In order to obtain total internal reflectance, the angle of incidence must exceed the critical angle defined as:

$$\theta_c = \sin^{-1}\left(\frac{n_2}{n_1}\right)$$

Where n_2 is the refractive index of the substances and n_1 is the refractive index of the crystal, and according to theory our current crystal configuration does not provide total internal reflectance. The refractive index of our substances pyrene (1.77), anthracene (1.729) and soot (1.92-1.98) combined with our refractive index and incident angle of our crystal, 2.4 and 45° respectively, we calculated an imaginary depth of penetration. Depth of penetration is defined as:

$$d_p = \frac{\lambda}{2\pi\left(n_1{}^2 sin^2\theta_1 - n_2{}^2\right)^{\frac{1}{2}}}$$

Where λ is the wavelength of the light (4000 cm^{-1} – 700 cm^{-1}), n_1 is the refractive index of the crystal, n_2 is the refractive index of the substance and θ_1 is the incident angle. To optimize the depth of penetration for our substances we can change θ_1 and/or the crystal substance. For anthracene to obtain the largest depth changing the crystal to AMTIR, a material produced as a glass from selenium, germanium and arsenic. AMTIR refractive

index of 2.5 and θ_1=45° gives a depth of penetration from 1.08 µm-6.14 µm. Pyrene and carbon (lampblack) can be optimized by increasing θ_1 to 60° for a ZnSe crystal, giving a penetration depth of .345µm-1.99µm for pyrene and 1.256 µm-2.839 µm for carbon (lampblack).

VITA

Name:	Laura Elizabeth Mason
Address:	Texas A&M Department of Atmospheric Sciences c/o Dr. Sarah Brooks 1204 Eller O&M, 3150 TAMU College Station, TX 77843-3150
Email Address:	lemason@tamu.edu
Education:	B.S., Meteorology, Texas A&M University, 2006 M.S., Atmospheric Sciences, Texas A&M University, 2009